Energy Conversion and Management 302 (2024) 118155

Contents lists available at ScienceDirect

Energy Conversion and Management

journal homepage: www.elsevier.com/locate/enconman

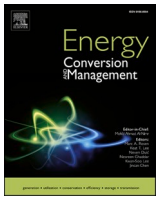

Wind forecasting-based model predictive control of generator, pitch, and yaw for output stabilisation – A 15-megawatt offshore

Tenghui Li [a], Jin Yang [a,*], Anastasia Ioannou [b]

[a] James Watt School of Engineering, University of Glasgow, Glasgow G12 8QQ, UK
[b] DTU Wind and Energy Systems, Roskilde DK-4000, Denmark

ARTICLE INFO

Keywords:
Model predictive control
Wind forecasting
Deep learning
Generator control
Pitch control
Yaw control

ABSTRACT

As wind energy continuously expands its share in power generation, the grid has a higher requirement for stable wind production. This study aims for a wind forecasting-based turbine control to mitigate power fluctuation caused by wind uncertainties. Firstly, a compass-vector transformation supports a wind model on direction forecasting besides velocity. Wind modelling adopts a general network structure of learning-shaping to learn the transformed vector series. Wind speed and direction averaged from prediction determine the three-degree-of-freedom (3-DOF) reference as the control objective and update the system configuration. Subsequently, the model predictive control (MPC) solves real-time regulation by sparse quadratic programming (QP). Besides, the control loop integrates generator control, speed compensation, and output buffer to coordinate the generator, pitch servo, and yaw servo. According to the simulation, the long short-term memory (LSTM) ensures a mean accuracy of over 0.997 on a 30-s prediction window. Its performance is more stable than the dense (DNN), convolutional (CNN), and CNN-LSTM. Compared to the baseline control, the proposed MPC can reduce 7% output oscillation and 12% peak-to-peak. Wind forecasting improves rotation and power stability by 44% at high wind. The proposed turbine control is proven to contribute to better wind power quality.

1. Introduction

With more attraction to low-carbon emissions, wind energy has experienced rapid development in technology and industrial applications in the past two decades [1]. Wind turbines (WTs), the device of the wind energy conversion system (WECS), are responsible for capturing wind energy and outputting electricity [2]. Turbine control performance dominantly influences output power quality [3]. However, wind uncertainties and aerodynamic nonlinearities induce control disturbance, leading to output fluctuation and grid supply risk [4]. This research intends to develop a control framework to forecast wind variation and utilize wind prediction to optimise configuration.

The primary type of WT is a three-degree-of-freedom (3-DOF) system that varies rotor speed, pitch angle, and yaw angle [5]. Wind forecasting provides a necessary wind reference that determines the 3-DOF objective, so a reliable wind model is critical for output stability [6]. Conventional wind forecasting involves physical and statistical models [7]. Physical models, a part of numerical weather prediction (NWP), take multiple meteorological and topographical parameters as input and calculate potential wind variation through physical laws [8]. Statistical methods analyse historical data to estimate wind distribution that calculates the most likely wind [9]. However, physical models are commonly expensive and slow in computation due to fluid calculations, e.g., the Navier-Stokes equation [10]. Statistical methods have a requirement of the stationary process [1] that is too strict to satisfy for short-term time series. In contrast, machine learning provides an efficient calculation with no prerequisite for series distribution [1].

Owing to the development of artificial intelligence techniques, machine learning favours employing deep-learning structures, such as convolutional neural network (CNN) and recurrent neural network

Abbreviations: CNN, convolution neural network; NWP, numerical weather prediction; DNN, dense neural network; PID, proportional integral derivative; DOF, degree of freedom; PMSG, permanent magnetic synchronous generator; IEA, International Energy Agency; PRPT, power reference point tracking; LQR, linear quadratic regulator; QP, quadratic programming; LSTM, long short-term memory; R^2, r-square; MAE, median absolute error; RMSE, root mean squared error; MLP, multilayer perceptron; RNN, recurrent neural network; MPC, model predictive control; SMC, sliding mode control; MPPT, maximum power point tracking; TSR, tip speed ratio; MSE, mean squared error; WECS, wind energy conversion system; NREL, National Renewable Energy Laboratory; WT, wind turbine.

* Corresponding author.
E-mail address: Jin.Yang@glasgow.ac.uk (J. Yang).

https://doi.org/10.1016/j.enconman.2024.118155
Received 3 November 2023; Received in revised form 30 December 2023; Accepted 27 January 2024
Available online 6 February 2024

(RNN), to achieve higher accuracy for time series forecasting, besides conventional multilayer perceptron (MLP) [11]. Neshat et al. proposed an evolutionary decomposition and a generalised normal distribution optimisation to enhance bidirectional long short-term memory (LSTM) for wind speed prediction [12]. Chen et al. introduced a novel hybrid CNN-LSTM architecture for wind speed forecasting, which encodes high dimensional input into embedding vectors and decodes prediction results [1]. Ahmed et al. employed an ensemble-based LSTM to investigate seasonal and periodic characteristics over wide data segmentations (3-month ~ 1-day) and time horizons (14-day ~ 5-minute) [13]. Xiang et al. combined a self-attention temporal CNN and an LSTM to forecast ultra-short-term wind power [14]. Liu et al. applied error correction and variational model decomposition into a hybrid CNN-LSTM-MLP for hourly solar irradiance prediction [11]. Ewees et al. adopted a human-behaviour-based metaheuristic algorithm, a heap-based optimiser, to train the LSTM, thus improving LSTM accuracy on wind power forecasting [15]. Agga et al. studied deep-learning architectures in photovoltaic power forecasting and suggested that the CNN-LSTM suppresses standard machine learning and single deep-learning models [16]. Fu et al. presented a framework of outlier processing, mode decomposition, subsequence reconstruction, and stacked generalization for short-term wind speed forecasting [17]. Also, data filtering and mode decomposition are helpful tools that can improve model training for complex series with the aid of nonlinearity identification, noise cleaning, and information extraction [18]. Although diverse state-of-the-art models continuously improve the reliability and accuracy of time series, their prediction window is too long for a turbine control system to update the control objective. In addition, most wind forecasting methods focus on wind speed but ignore direction. This work targets seconds-level deep learning for wind speed and direction series.

When a wind model predicts speed and direction, an operational optimisation will transform wind reference to the proper rotation, pitch, and yaw (3-DOF) [19]. Modern turbine control relies on maximum power point tracking (MPPT), in which wind generation crosses a variable speed region (Region ii) and a pitch regulation region (Region iii) [20]. However, the conventional MPPT is not flexible for large-capacity WTs. This research also introduces a dynamic operation optimisation driven by the wind model to update the 3-DOF reference for the controller. After that, turbine control executes different 3-DOF operations and deals with disturbances caused by wind stochastics. Gambier and Meng designed a proportional-integral-derivative (PID) 20-megawatt (MW) system that considers torque control, pitch control, and fore-aft damping [21]. Kelkoul and Boumediene proposed a sliding mode control (SMC) enhanced by a super-twisting algorithm to reduce generator chattering [22]. Li et al. developed a linear quadratic regulator (LQR) that coordinates generator and pitch servo responses through forecasted aerodynamics [23]. Sudharsan et al. presented a pseudo-adaptive model prediction control (MPC) integrating torque and pitch control for fatigue mitigation [24]. The MPC is more promising among existing controllers because its horizon prediction contributes less control cost and more robust adaptability. Various controllers make efforts for higher control performance, but most do not consider wind forecasting to predict future wind variations and adjust their control objectives in advance. This work will combine the wind forecasting model and the MPC to enhance stability and reduce output fluctuation.

This study aims for a wind forecasting-based MPC design and has the following contributions:

The proposed wind forecasting method processes the time series of wind horizontal and vertical components instead of directly passing wind series so that the forecasting model can handle wind speed and direction.

Four deep models (MLP, CNN, LSTM, and CNN-LSTM) take a general structure of learning-shaping to be compatible with wind vector series. Meanwhile, four models are tested and compared for the prediction performance.

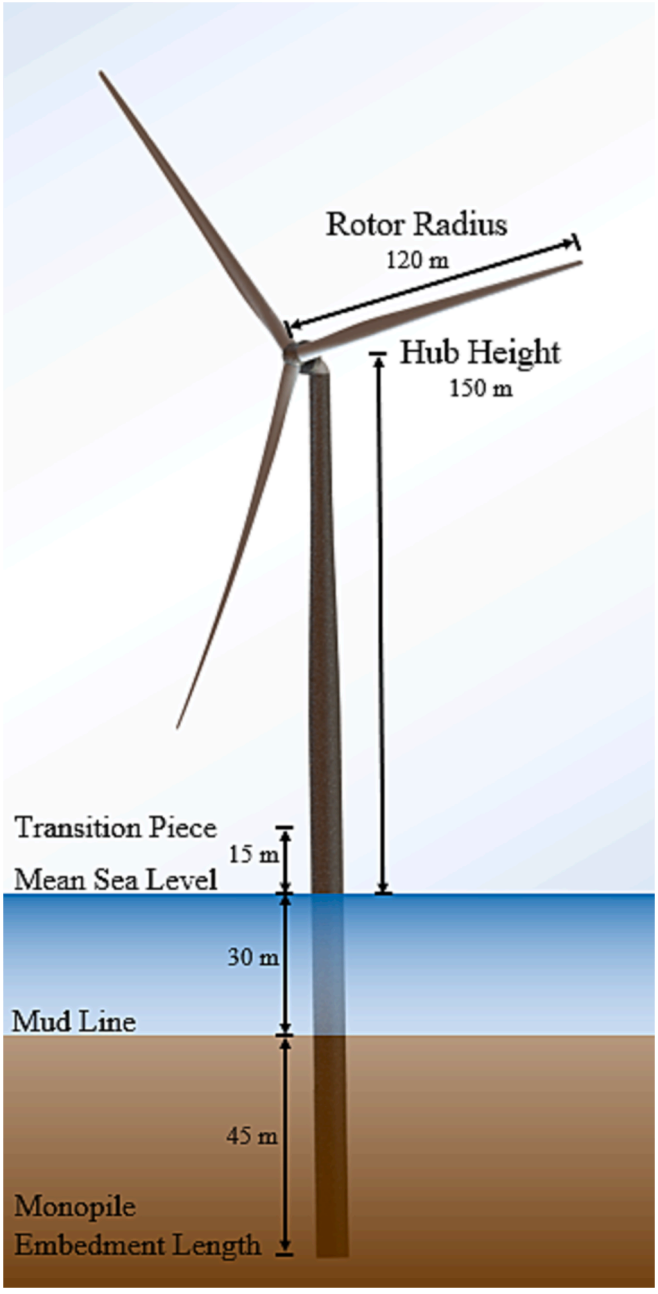

Fig. 1. The IEA 15-MW offshore reference.

An operation optimisation algorithm receives the weighted wind reference forecasted by the wind model and determines the optimal working point to capture the nominated power. This procedure derives necessary speed, pitch, and yaw references as the control objective.

The MPC updates its internal system model according to wind prediction and initializes the regulation problem. A more accurate system model improves the aerodynamic estimation of the MPC, which benefits better control accuracy and robustness.

The forecasting-enhanced MPC incorporates generator, pitch, and yaw control, which has a global regulation of 3-DOF. The highly integrated MPC conduces to a fully coupled system that balances different components to optimise the control reaction.

This paper organizes the contents as follows. **Section 2** introduces the target turbine and flowchart. **Section 3** demonstrates wind series

Table 1
Parameters of the IEA 15-MW offshore.

Parameter	Value	Comment
Wind turbine class	IEC class 1B	–
Rotor orientation	upwind	–
Control	variable speed collective pitchnacelle rotation	updated to variable power controlcompatible with maximum energy capture
Cut-in wind speed	4.4 m/s	optimised to avoid too low outputs
Cut-off wind speed	25 m/s	–
Rated wind speed	10.2 m/s	optimised for perpendicular rotation plane
Power rating	15 MW	–
Number of blades	3	–
Rotor diameter	240 m	–
Airfoil series	FAA-W3	50 blade elements
Minimum rotor speed ω_d^{min}	5.0 RPM	–
Maximum rotor speed ω_d^{max}	7.56 RPM	–
Design pitch β_{min}	0 deg	minimum pitch angle
Pitch time constant τ_β	1 s	first-order model
Pitch velocity β_v	7 deg/s	maximum velocity
Yaw time constant τ_γ	1.5 s	first-order model
Nacelle rotation limit γ_v	0.25 deg/s	maximum rotation
Blade mass	65,000 kg	corresponds to a moment of inertia$J_t = 936,000,000\,\mathrm{kg} \bullet \mathrm{m}^2$
Shaft driving	direct drive	accounts for zero damping$D_t = 0\mathrm{N} \bullet \mathrm{m}/\mathrm{rad} \bullet \mathrm{s}$
Number of pole pairs p	100	matched for 7.56 RPM
Stator voltage V_g	4.77 kV	–
Stator resistance R_s	0.16 Ω	–
Stator d-axis inductance L_d	0.01587H	$L_d = L_q$ for symmetrical machines
Stator q-axis inductance L_q	0.01587H	–
Permanent magnet flux F_f	19.49 wb	–
Electrical frequency f_e	12.6 Hz	–
Generator efficiency k_g	96.5 %	mechanical efficiency

modelling with four deep networks and derives 3-DOF references from wind prediction. **Section 4** details the forecasting-based MPC, including real-time system modelling, quadratic programming (QP), and control loop of the generator, pitch servo, and yaw servo. **Section 5** examines model accuracy and control performance. **Section 6** summarizes the main findings and conclusions.

2. Overview

With moving into the deep ocean, offshore WTs have a range of capacity in rated power from 8 MW to 20 MW, in which the share of 15 to 20 MW has reached 38 % [25]. As the main steam offshore in the recent decade, the 15-MW turbine is worth investigating for industrial applications. The section will introduce a 15-MW reference and illustrate the overall design of the reference turbine.

2.1. Target turbine

The National Renewable Energy Laboratory (NREL) and the Technical University of Denmark report a reference WT of 15-MW through the second work package of the International Energy Agency (IEA) wind task 37, named IEA 15-MW [5]. The IEA 15-MW leaps ahead of the present generation of industry WTs for fixed-bottom offshore wind energy. The IEA 15-MW applies a monopile support structure, a Class IB direct-drive machine, a rotor diameter of 240 m, and a hub height of 150 m, as displaced in Fig. 1 [5]. This study will use the IEA 15-MW to implement and discuss the proposed control design.

Table 1 provides the necessary parameters of the IEA 15-MW. Each simulation step iterates on 50 blade elements of the IEA 15-MW to compute aerodynamic responses. The IEA 15-MW employs a 200-pole permanent magnetic synchronous generator (PMSG) to absorb shaft kinetic energy and convert it to electrical power. The rated output of the PMSG (15 MW) corresponds to 96.5 % of absorbed rotation energy. Besides, the first-order model with rate constraint mathematically simulates pitch and yaw servos.

2.2. Design flowchart

Large-size WTs favour a direct-drive design that implants the rotor shaft to the generator rotor, which benefits a compact nacelle space. Fig. 2 is the direct-drive profile of the IEA 15-MW that consists of the PMSG, pitch servo and yaw servo. The proposed control framework consists of wind forecasting and control optimisation. The forecasting module takes wind velocity and direction measurements from an anemometer and a vane mounted on the turbine nacelle. Subsequently, the vector series converted from the wind measurement is passed to a wind vector series model to predict future wind vectors. The inverse vector transformation restores the predicted wind speed and direction. The processing unit will use the wind prediction to configure the working point (rotation, pitch, yaw, and captured power). Meanwhile, the control module updates the system model that linearizes the coupled response at the working point. After that, the MPC initializes its regulation model and objective to monitor the system state and react to state transition or perturbation.

3. Wind forecasting

Wind forecasting uses several prior wind samples to predict future wind trends as time series forecasting. An accurate forecasting model ensures the optimal control configuration for higher system stability and power quality. This section will build four networks to predict wind vector series through data preprocessing and compass-vector transformation, as shown in Fig. 3.

3.1. Data description

Since multiple variables might affect wind prediction, it is necessary to perform a feature selection to include proper features for time series modelling [26]. Considering the employed dataset gathered from multi-meteorological sensors has 13 variables, the spatial correlation [7] between these features evaluates their dependencies. A negative correlation means an opposite variation between two series candidates, but its magnitude means the same correlation intensity as a positive. Therefore, Fig. 4 calculates the absolute correlation for feature analysis, in which a value close to the unit shows a higher correlation. Air pressure (barometer measurements) correlates lightly with wind velocity and direction, and temperature potentially affects direction, but both correlations are less than 0.5. Only wind measurements at different heights have strong correlations. Hence, the time series modelling ignores air pressure and temperature and only considers wind velocity and direction at the hub height for simplicity.

Fig. 5 defines the representation of wind measurement in the compass direction, which is clockwise and represents the direction blowing from [9]. Angles are not explicit model inputs due to 0° or 360° alternations. For better learning, a vector decomposition transforms wind velocity v_i and direction θ_v as **Eqs. (1)(2)**, with inverse transformation as **Eqs. (3)(4)**.

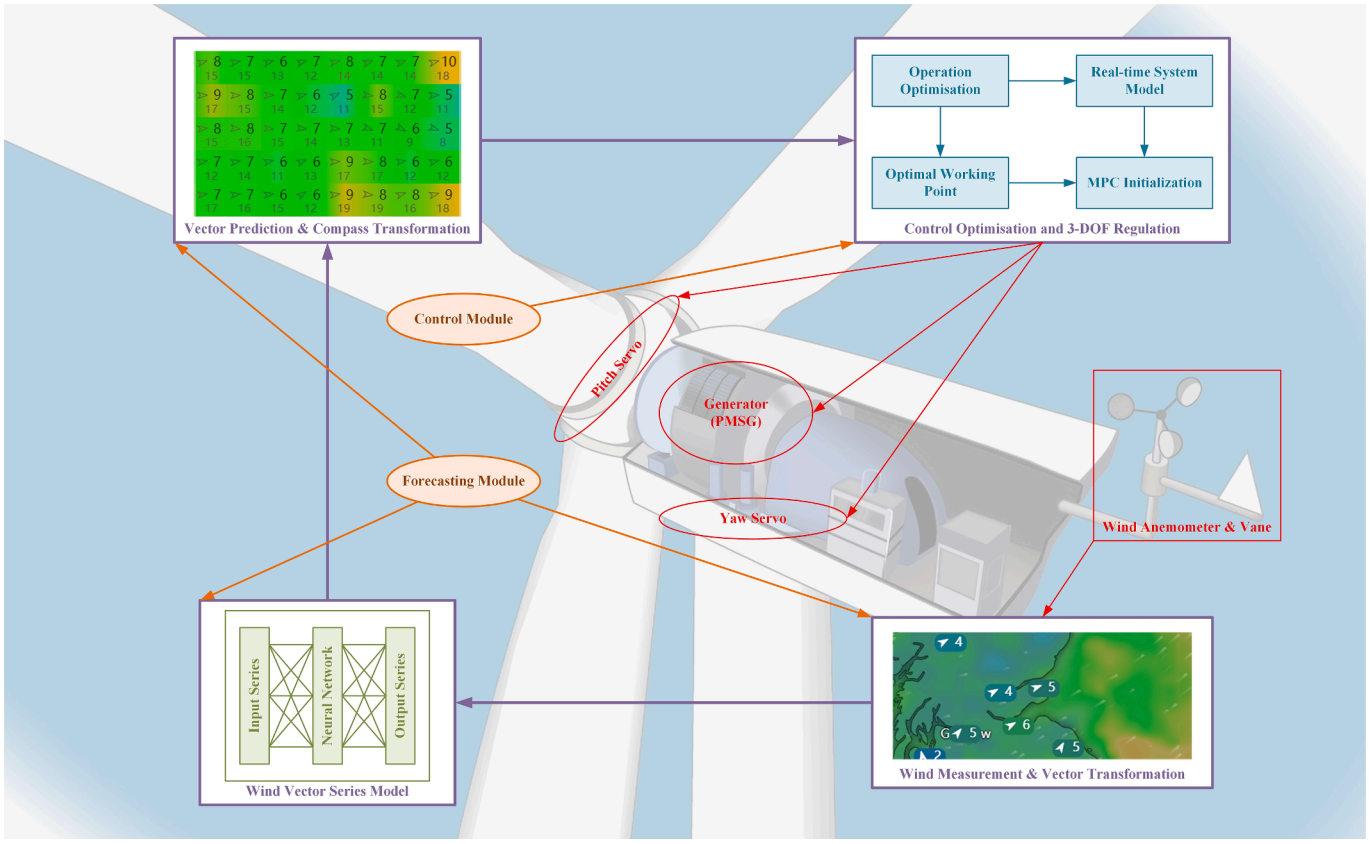

Fig. 2. The flowchart from wind forecasting to control optimisation.

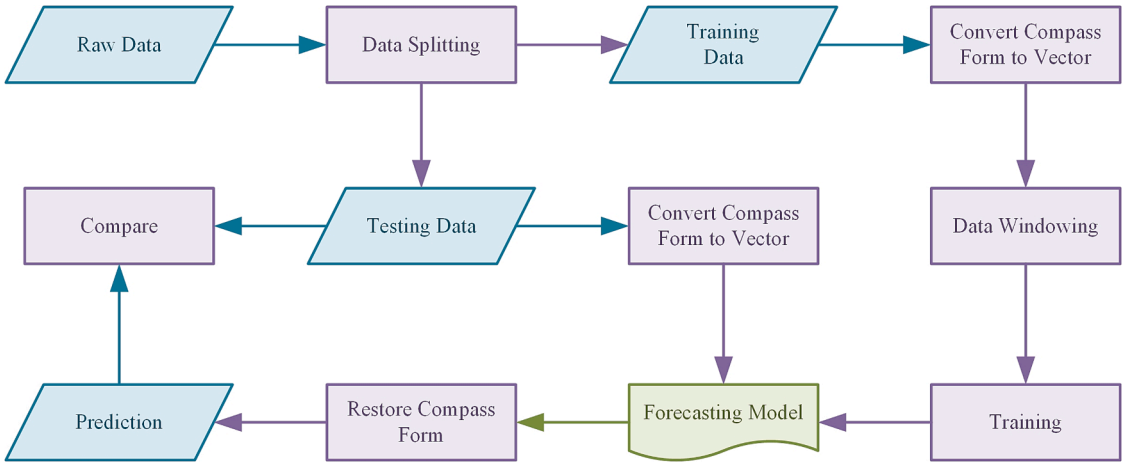

Fig. 3. Procedures of training and testing a wind series model.

$$v_x = v_i \bullet \cos\theta_v \tag{1}$$

$$v_y = v_i \bullet \sin\theta_v \tag{2}$$

$$v_i = \sqrt{v_x^2 + v_y^2} \tag{3}$$

$$\theta_v = \arctan\frac{v_x}{v_y} \tag{4}$$

Fig. 6 compares the distribution of the joint velocity and direction and the decomposed vector. It clearly shows wind vectors are much simpler for the model to learn. Therefore, wind forecasting converts compass wind to wind vector and later returns to compass wind after forecasting. Meanwhile, a forecasting model no longer needs to weigh input features because an orthogonal pair have equal importance.

The training set has 2,281,610 samples sampled at a frequency of 0.1-Hz. Table 2 summarises statistics of the training set about compass and vector. Velocities concentrate on 4.28 ~ 9.62 m/s, and directions focus on about 90° and 250° affected by seasonal winds. Model testing is on a successive 30-day set of 259,200 samples.

3.2. Preprocessing

For passing correct information into a model, the min–max scaler (**Eqs. (5)(6)**) performs input normalization and prediction restoration

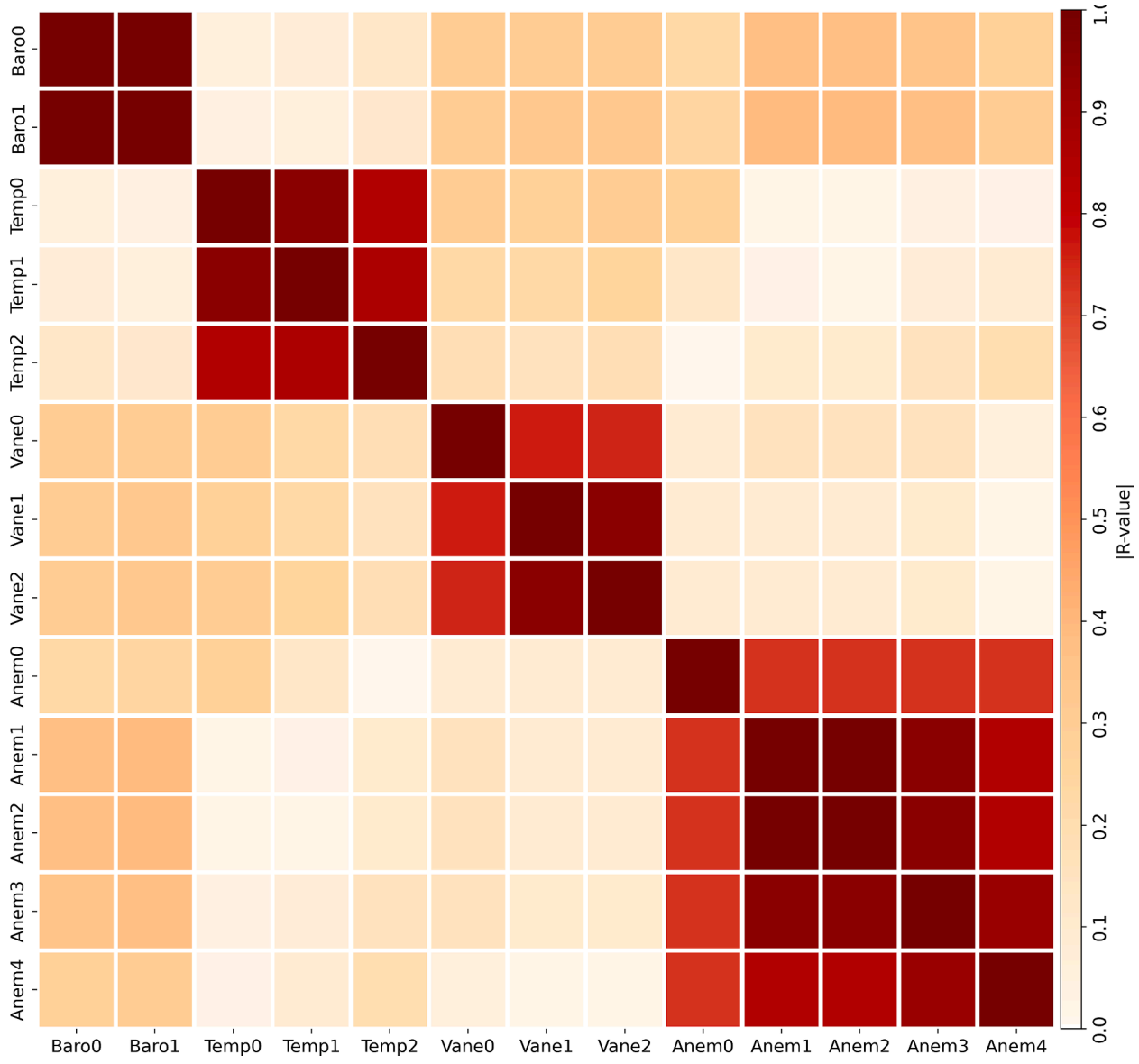

Fig. 4. Heatmap of the spatial correlation between features including barometer, temperature, wind vane, and wind anemometer.

[27]. $\widetilde{x} = \left[v_x,\ v_y\right]^{\mathrm{T}}$ is an orthogonal vector, $\widetilde{x}_{min}$ and $\widetilde{x}_{max}$ can be found in Table 2.

$$\widetilde{x}' = \frac{\widetilde{x} - \widetilde{x}_{min}}{\widetilde{x}_{max} - \widetilde{x}_{min}} \tag{5}$$

$$\widetilde{x} = \widetilde{x}' \bullet \left(\widetilde{x}_{max} - \widetilde{x}_{min}\right) + \widetilde{x}_{min} \tag{6}$$

Windowing is a way to process time series data so that a machine learning platform can perform training on inputs and prediction labels to make a time series model. Meanwhile, a windowing definition determines the time axis of successive predictions. Fig. 7 visualizes windowing operation on training and testing sets. A complete window consists of input and shift subwindows, in which a shift subwindow includes an offset and a label. The green offset in Fig. 7 is for flexible applications, such as reserving time for model calculation. It notes that the proposed windowing has different movements on training and testing sets. Each window from the training set is independent and has no overlap with adjacent windows. However, the testing set moves the window according to the label width to make successive predictions. In this study, an input subwindow of 6 samples and a label subwindow of 3 predictions constitute a window without offset.

3.3. Deep learning models

Deep learning models rely on complex and multiple network architectures that exploit nonlinear mapping capabilities [28]. The convolutional and recurrent structures are the two most widely applied deep-learning methods in time series forecasting [11]. This section will introduce CNN and LSTM-based models to predict 2-D wind vector series. Meanwhile, wind modelling includes an MLP and a hybrid CNN-LSTM for comparison. Under the window definition, four models have the same input shape of 6×2 and output shape of 3×2, corresponding to a sampled 60-s input series and a forecasted 30-s label series. In other words, a wind forecasting model predicts half a minute for the control optimisation. Model training and replay uses Tensorflow [29]. The gradient optimiser is the Adam optimiser [30], and the loss function is the mean squared error (MSE) [31].

3.3.1. Dense neural network

The DNN is a classic type that stacks regular layers in Tensorflow

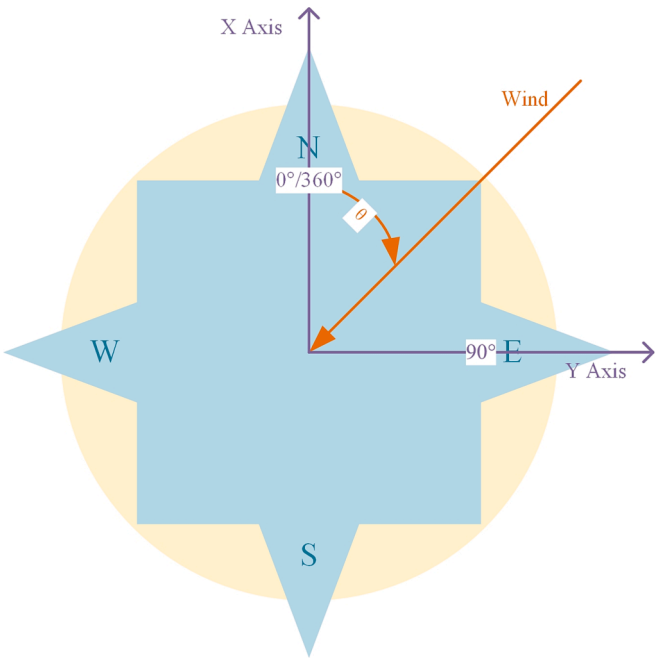

Fig. 5. Compass wind reporting velocity and direction (the north refers to 0° or 360°).

[29]. The DNN is another name for deep-learning MLP, one of the primal deep-learning neural networks. The developed DNN is a seven-layer architecture, as illustrated in Fig. 8. The hidden part between input and label layers undertakes two tasks: one is for learning underlay time series information, and the other is for shaping so that a prediction has an expected output shape, which yields a learning-shaping structure.

Since the native dense layer only works for 1-D vectors, it requires flattening the 2-D input layer to pass data flow correctly. All dense layers for learning take the ReLU [14] as their activation function to introduce nonlinearity between connected layers. In the shaping structure, the dense layer whose neurons equal the label size applies the linear operation to achieve direct output, and the reshaping layer transforms the hidden vector into the label shape. It notes that the shaping structure is reused in the following networks to achieve 2-D prediction.

Table 3 gives specific layer configurations in Tensorflow. The hyperparameter tuning of the DNN neurons only adjusts four dense layers on the learning side. Their neurons can be equally increased or decreased with a step of 16 units until the training loss converges smoothly. The tuning of the other models also follows the same principle. The configuration of Table 3 can ensure steady training through multiple trials. It is worth mentioning that a robust network should not be sensitive to hyperparameters. It should consider adding a learning layer if similar hyperparameters lead to enormous prediction discrepancies.

3.3.2. *Convolutional neural network*

The CNN has become a primary deep-learning method in renewable energy forecasting [11]. It relies on feature extraction to interpret a sophisticated data topological structure, which has achieved success in image processing [11]. Compared with 2-D images, the only difference in applying the CNN in wind series forecasting is that a convolution kernel convolves the input layer on a single spatial (or temporal) dimension [1]. Fig. 9 is the CNN architecture in this study. The 1-D convolution layer moves the kernel window along with the time axis of the input series. Since the Conv1D layer has parsed the underlay time information, the unfolded Conv1D output cascades a dense layer for learning.

Table 4 details the optimised structure of Fig. 9. The convolution and flattening layers perceive time series features and output a character vector so that a dense layer can understand temporal characteristics. It accounts for plenty of neurons in the dense layer on the learning side.

Table 2
Description of 0.1-Hz wind training data.

	Mean	Std.	Min.	25 %	50 %	75 %	Max.
v_i(m/s)	7.30	3.97	−0.10	4.28	6.89	9.62	33.71
θ_v(°)	192.97	87.40	0.01	110.36	218.62	259.84	359.99
v_x(m/s)	−1.19	4.80	−24.64	−3.95	−1.24	1.23	17.98
v_y(m/s)	−1.64	6.47	−28.53	−6.66	−2.16	3.19	24.68

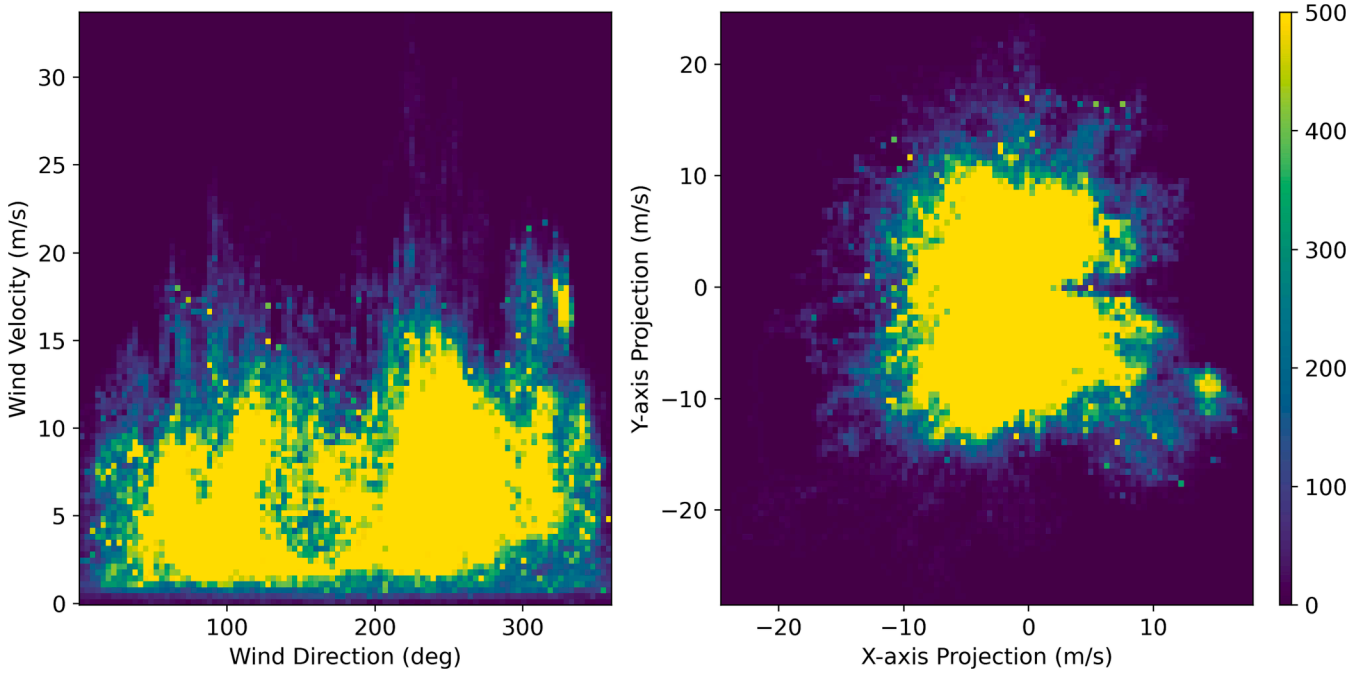

Fig. 6. Wind distribution (uneven relation between velocity and direction) and vector decomposition (uniform relation).

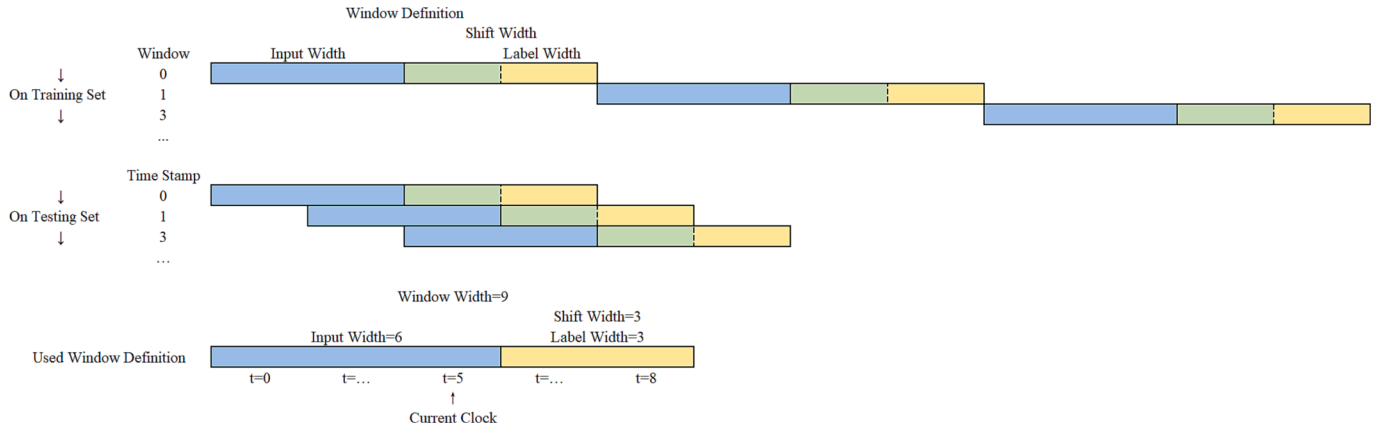

Fig. 7. Window definition for sampling and forecasting.

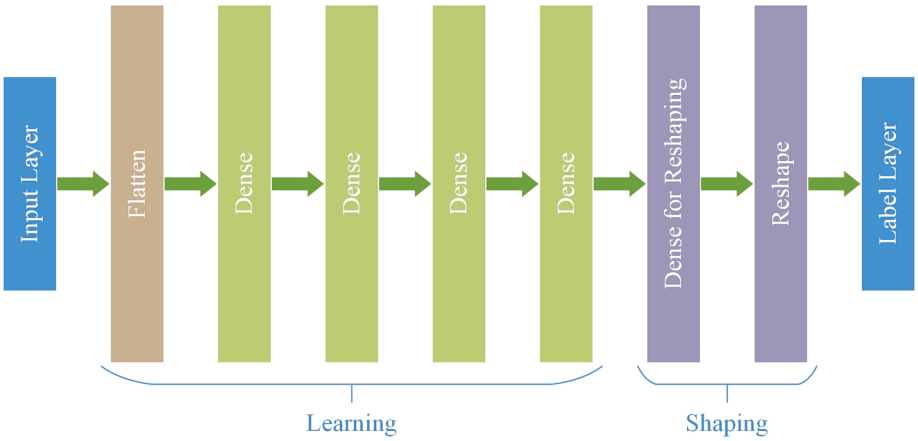

Fig. 8. The structure of stacked dense layers.

Table 3
The DNN configuration.

Layer	Arguments	Value	Parameters
Flatten	–	–	–
Dense	unitsactivation	32relu	416
Dense	unitsactivation	32relu	1,056
Dense	unitsactivation	32relu	1,056
Dense	unitsactivation	32relu	1,056
Dense	units	6	198
Reshape	–	(3, 2)	–

3.3.3. *Long short-term memory*

The LSTM is one of the most popular extensions of the RNN that predicts various time series [11]. The basic mechanism of a recurrent structure is a sequential model that can arrange time-series data as input vectors and supply output results through its internal cell [15]. Therefore, the input series goes through cells in a sequential vector, and the output label concatenates with the next time series at each movement [13]. The LSTM uses memory cells (Fig. 10) to replace conventional RNN cells, thus solving the gradient explosion and disappearance of the RNN.

Assuming the forget gate f_t, input gate i_t, cell state C_t, and output gate o_t in Fig. 10, **Eqs. (7)~(12)** represent the calculation procedure of the LSTM at each step [1]. The input gate controls the information received by memory cells, the output gate controls the forecasted information of memory cells, and the forget gate determines the information to be removed [9]. Memory cells are responsible for recording cell states [9].

$$f_t = \sigma\left(W_f \bullet [h_{t-1},\ x_t] + b_f\right) \tag{7}$$

$$i_t = \sigma(W_i \bullet [h_{t-1},\ x_t] + b_i) \tag{8}$$

$$C_t^{'} = \tanh(W_C \bullet [h_{t-1},\ x_t] + b_C) \tag{9}$$

$$C_t = f_t{*}C_{t-1} + i_t{*}C_t^{'} \tag{10}$$

$$o_t = \sigma(W_o \bullet [h_{t-1},\ x_t] + b_o) \tag{11}$$

$$h_t = o_t{*}\tanh(C_t) \tag{12}$$

where W and b are the weight and bias of a gate/cell. The LSTM with the shaping structure adopts the setting of Table 5.

3.3.4. *Hybrid network*

This section combines a CNN and an LSTM to build a hybrid CNN-LSTM model. Fig. 11 illustrates the whole framework. In the hybrid model, the CNN plays a role in feature extraction, and the LSTM works as a temporary forecasting layer to calculate such extracted features along the time axis. Therefore, the LSTM undertakes forecasting functionality for extracted features, not raw time series. The CNN-LSTM structure is supposed to be an encoder-decoder mechanism in which the CNN is the encoder, and the LSTM is the decoder [1].

Table 6 lists the layer configuration of the CNN-LSTM. Owing to recurrent prediction, the CNN-LSTM still has a concise layer structure. However, the LSTM layer requires more parameters waiting for training because extracted features increase the LSTM input dimension.

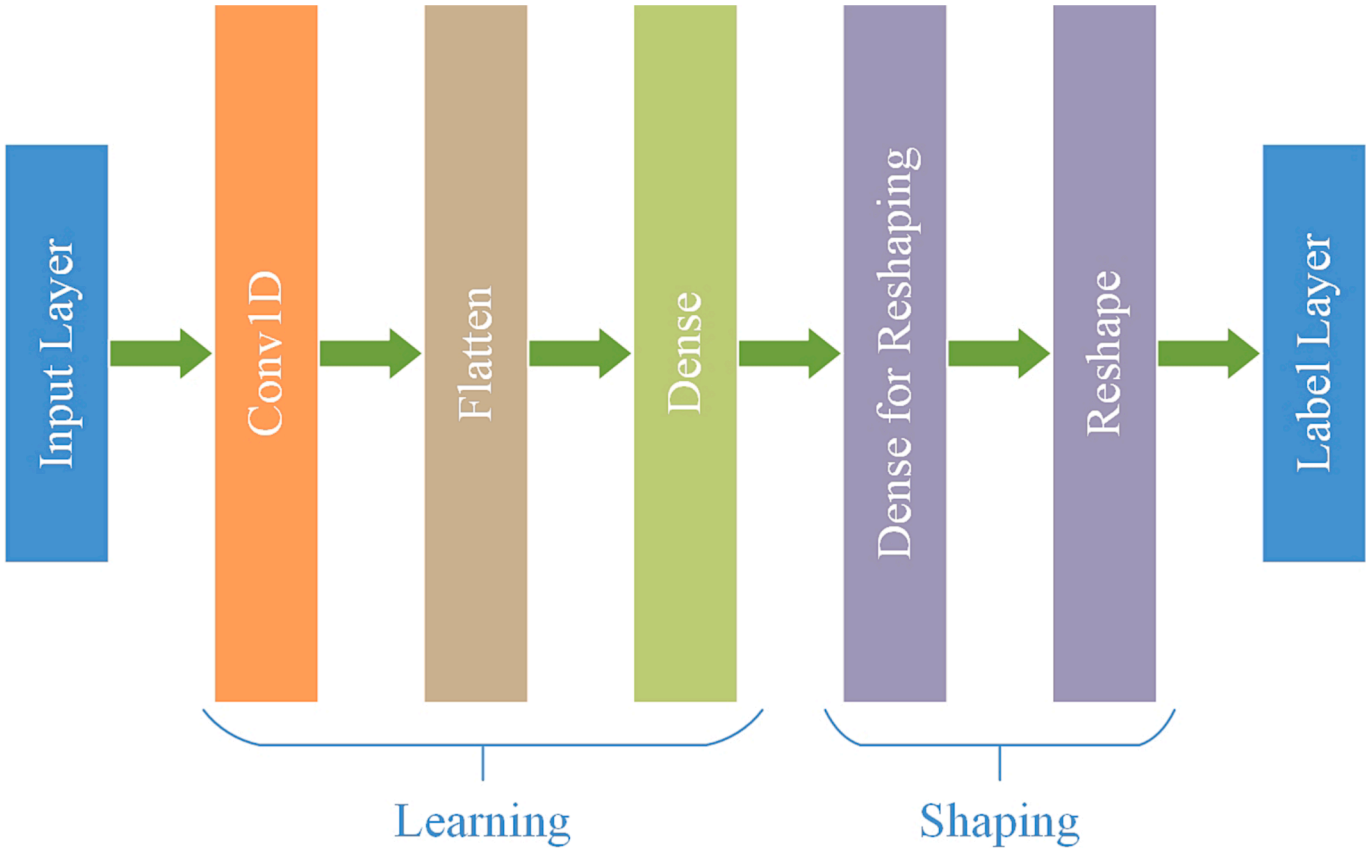

Fig. 9. The 1-D convolutional structure.

Table 4
The CNN configuration.

Layer	Arguments	Value	Parameters
Conv1D	filters	32	224
	kernel size	3	
	activationpadding	relusame	
Flatten	–	–	–
Dense	unitsactivation	32relu	6176
Dense	units	6	198
Reshape	–	(3, 2)	–

3.4. Evaluation criteria

Model evaluation adopts three indexes: the r-square (R^2, **Eq. (13)**) [30], the median absolute error (MAE, **Eq. (14)**) [15], and the root mean squared error (RMSE, **Eq. (15)**) [27]. The R^2 is a correlation coefficient that measures consistency between model predictions and measurements. The MAE focuses more on the central part of data distribution and eliminates the influence of some exceptional cases from the head and tail. The RMSE is a classic statistical metric that indicates the divergence of the group error of forecasted values.

$$R^2 = 1 - \frac{\sum_{i=1}^{N}(y_i - y_p)^2}{\sum_{i=1}^{N} y_p^2} \tag{13}$$

$$MAE = \text{median}\left(\left|y_i - y_p\right|\right) \tag{14}$$

$$RMSE = \sqrt{\frac{1}{N}\sum_{i=1}^{N}(y_i - y_p)^2} \tag{15}$$

where y_i is the i-th measurement and y_p is the corresponding model outcome.

3.5. Operation optimisation

After a wind model generates a series of wind vector predictions, a weighted average tool determines the average wind speed and direction in the label length as wind reference. Assuming averaged wind vectors ($\overline{v}_x$, $\overline{v}_y$), **Eqs. (16)(17)** compute wind speed and direction references. **Eqs. (17)(18)** weights wind components by assigning more importance to a closer prediction.

$$\overline{v}_i = \sqrt{\overline{v}_x^2 + \overline{v}_y^2} \tag{16}$$

$$\overline{\theta}_v = \arctan\frac{\overline{v}_x}{\overline{v}_y} \tag{17}$$

$$\overline{v}_x = \frac{\sum_{i=0}^{N-1}(N-i) \bullet v_i^x}{\sum_{n=1}^{N} n} \tag{18}$$

$$\overline{v}_y = \frac{\sum_{i=0}^{N-1}(N-i) \bullet v_i^y}{\sum_{n=1}^{N} n} \tag{19}$$

As the IEA 15-MW is an upwind WT, the nacelle orientation expects to face the wind flow, which infers the yaw reference equals the predicted direction. **Eqs. (20)~(22)** unwrap the yaw angle to make a continuous yaw orientation.

$$\gamma^+ = \text{mod}\left(\overline{\theta}_v - \gamma'_{ref},\ 2\pi\right) \tag{20}$$

$$\gamma^- = \gamma^+ - 2\pi \tag{21}$$

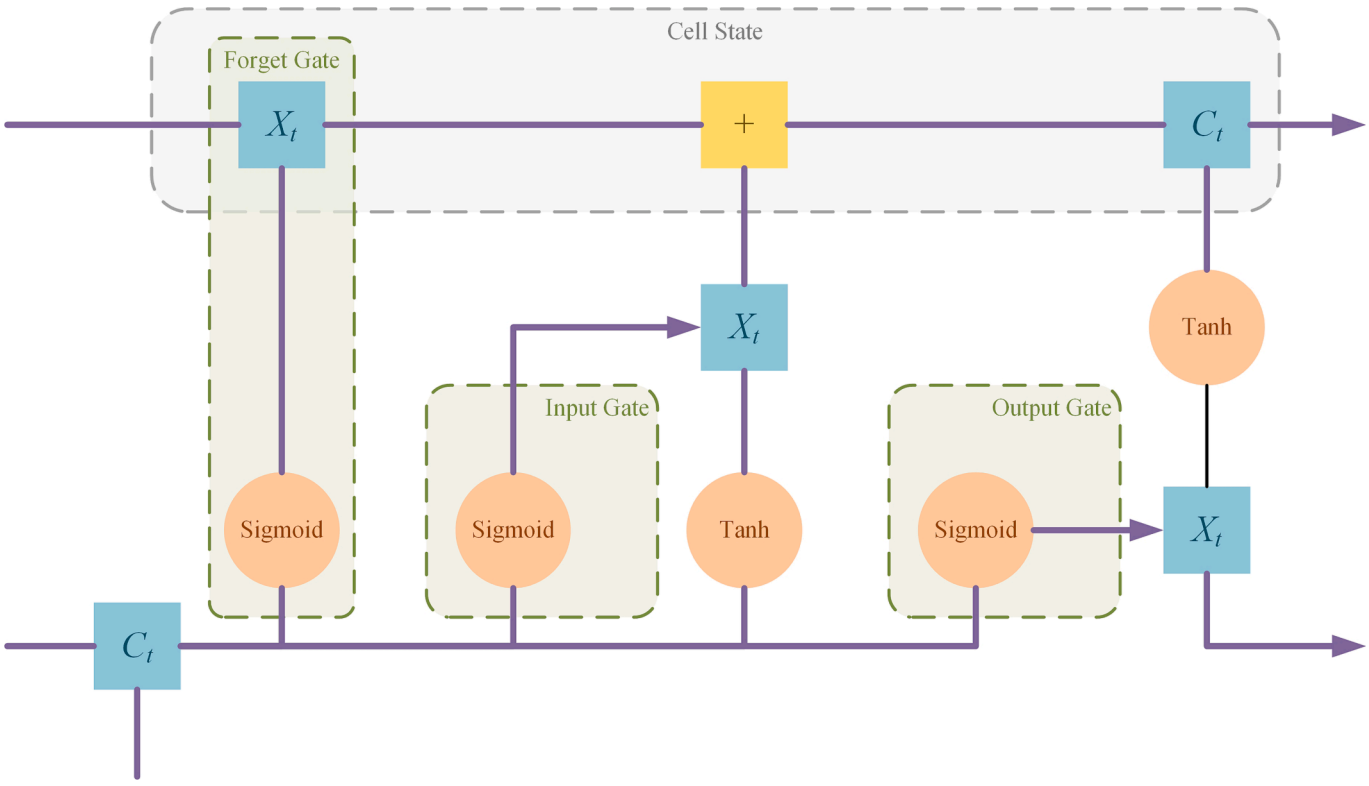

Fig. 10. The LSTM cell structure.

Table 5
The LSTM configuration.

Layer	Arguments	Value	Parameters
LSTM	units	32	4480
Dense	units	6	198
Reshape	–	(3, 2)	–

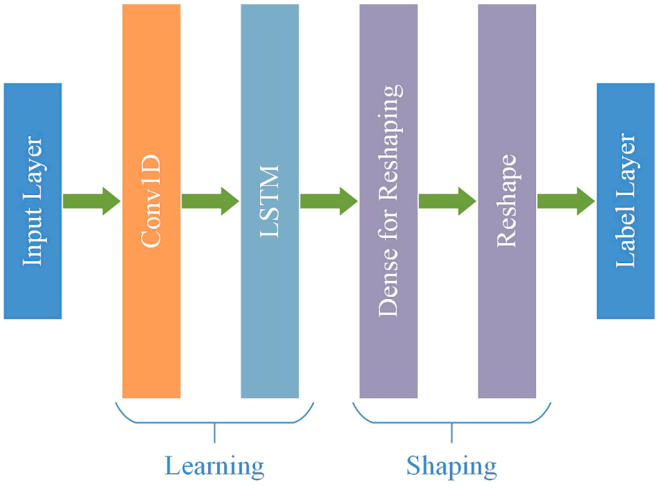

Fig. 11. The CNN-LSTM structure.

Table 6
The CNN-LSTM configuration.

Layer	Arguments	Value	Parameters
Conv1D	filters	32	224
	kernel size	3	
	activationpadding	relusame	
LSTM	units	32	8320
Dense	units	6	198
Reshape	–	(3, 2)	–

$$\gamma_{ref} = \begin{cases} \gamma'_{ref} + \gamma^{+}, & if\ \gamma^{+} < |\gamma^{-}| \\ \gamma'_{ref} + \gamma^{-}, & else \end{cases} \tag{22}$$

where γ'_{ref} denotes the last yaw reference. **Eqs. (20)(21)** calculate the rotation angle from clockwise or counterclockwise, and **Eq. (22)** selects the minimum rotation angle. After the above, the IEA 15-MW needs rotor speed and pitch angle references to determine power capture.

Most WT controllers are variants of the MPPT, i.e., receiving wind power as much as possible [32]. This research applies a control strategy that can vary output power to meet different generation requirements, i.e., power reference point tracking (PRPT) [23]. The PRPT operation requires a synthesis aerodynamic model of the IEA 15-MW that can provide power and torque response from wind velocity, rotor speed, and pitch angle. **Algorithm 1** takes advantage of the aerodynamic model and computes the operating point (ω_d^{ref}, β_{ref}, P_d^{ref}) for variable speed and pitch regulation [23]. It notes that **Algorithm 1** receives prediction $\bar{v}_i$ from **Eq. (16)** as input wind speed. The basic idea behind **steps 1 ~ 5** is to find the maximum load at the forecasted wind speed, which follows the optimal tip speed ratio (TSR) [33] and the pitch regulation rule of Region iii. Subsequently, **steps 6 ~ 10** try to pitch blades to reduce the captured power until it reaches the target power P_t. Finally, the

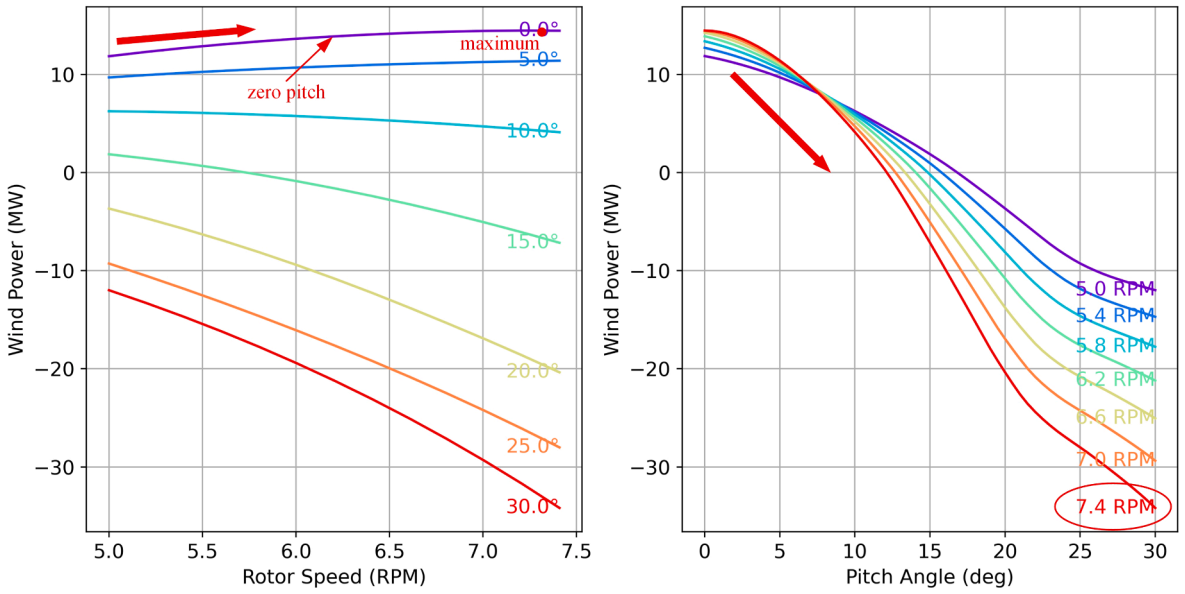

Fig. 12. Example of the rotor speed and pitch angle optimisation.

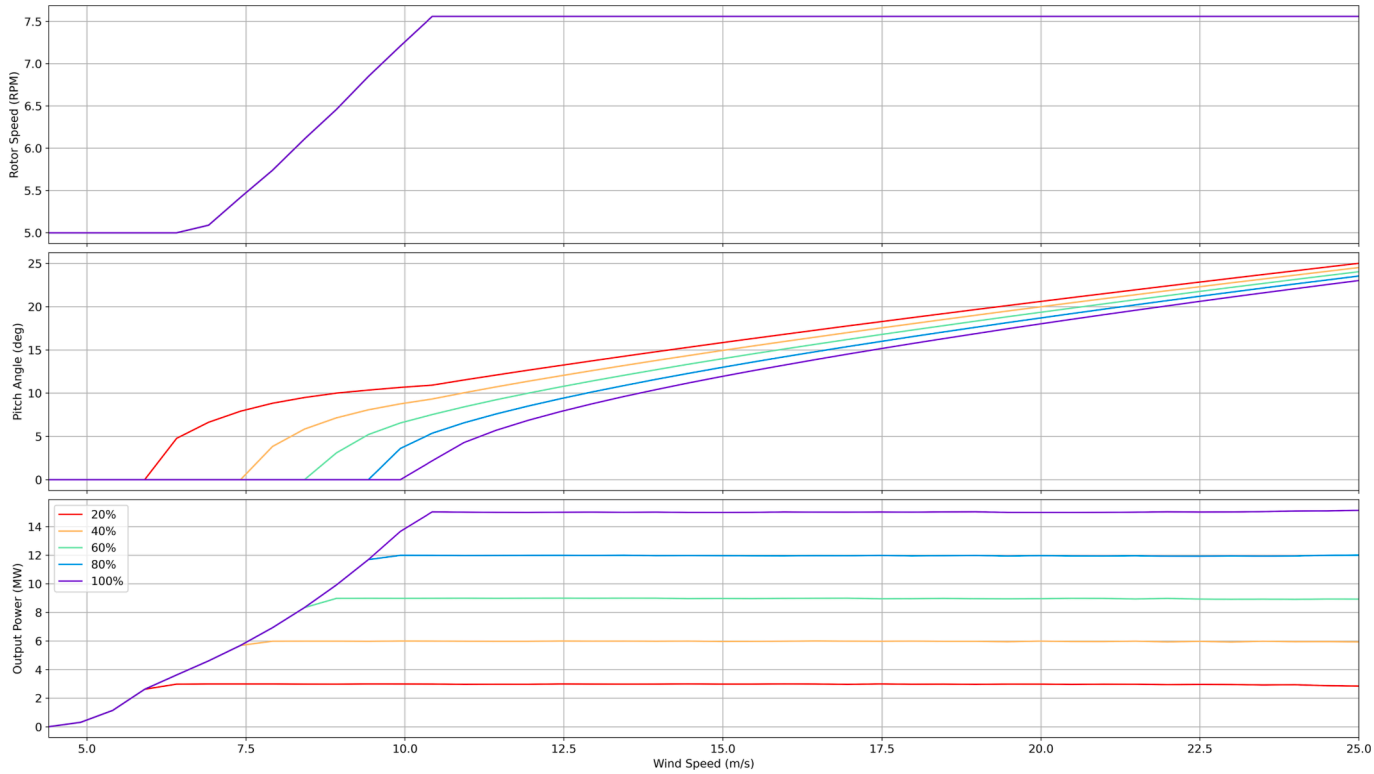

Fig. 13. Example of the power curve of the IEA 15-MW in the PRPT (overlapped speed curves due to the TSR, multiple angle curves for different targets).

algorithm returns reference values and torque sensitivities.

Algorithm 1. Control input reference optimisation

Input initialize rotor speed and pitch angle references (ω_d, β)load the IEA 15-MW aerodynamic model ($\mathscr{M} \leftarrow [v_i,\ \omega_d,\ \beta]$)
receive the external power output target P_t

Output speed, pitch, and power references (ω_d^{ref}, β_{ref}, P_d^{ref})torque sensitivities ($\frac{\partial Q_d}{\partial \omega_d}$, $\frac{\partial Q_d}{\partial \beta}$)

1. **if** in Region ii:

(*continued on next column*)

(*continued*)

Algorithm 1. Control input reference optimisation

2. find $\omega_d^{ref} = \omega_d$
   where $\mathscr{J}(\omega_d) = \max\left(\mathscr{M}|_{P_d}\right)$ with $\beta = \beta_{min}$
3. **else** (Region iii):
4. find $\beta_{ref} = \beta$
   where $\mathscr{J}(\beta) = \min\left(\text{abs}\left(\mathscr{M}|_{P_d} - P_d^{max}\right)\right)$ with $\omega_d = \omega_d^{max}$
5. predict the maximum power $P_d^{max} \leftarrow \left[v_i,\ \omega_d^{ref},\ \beta_{ref}\right]$

(*continued on next page*)

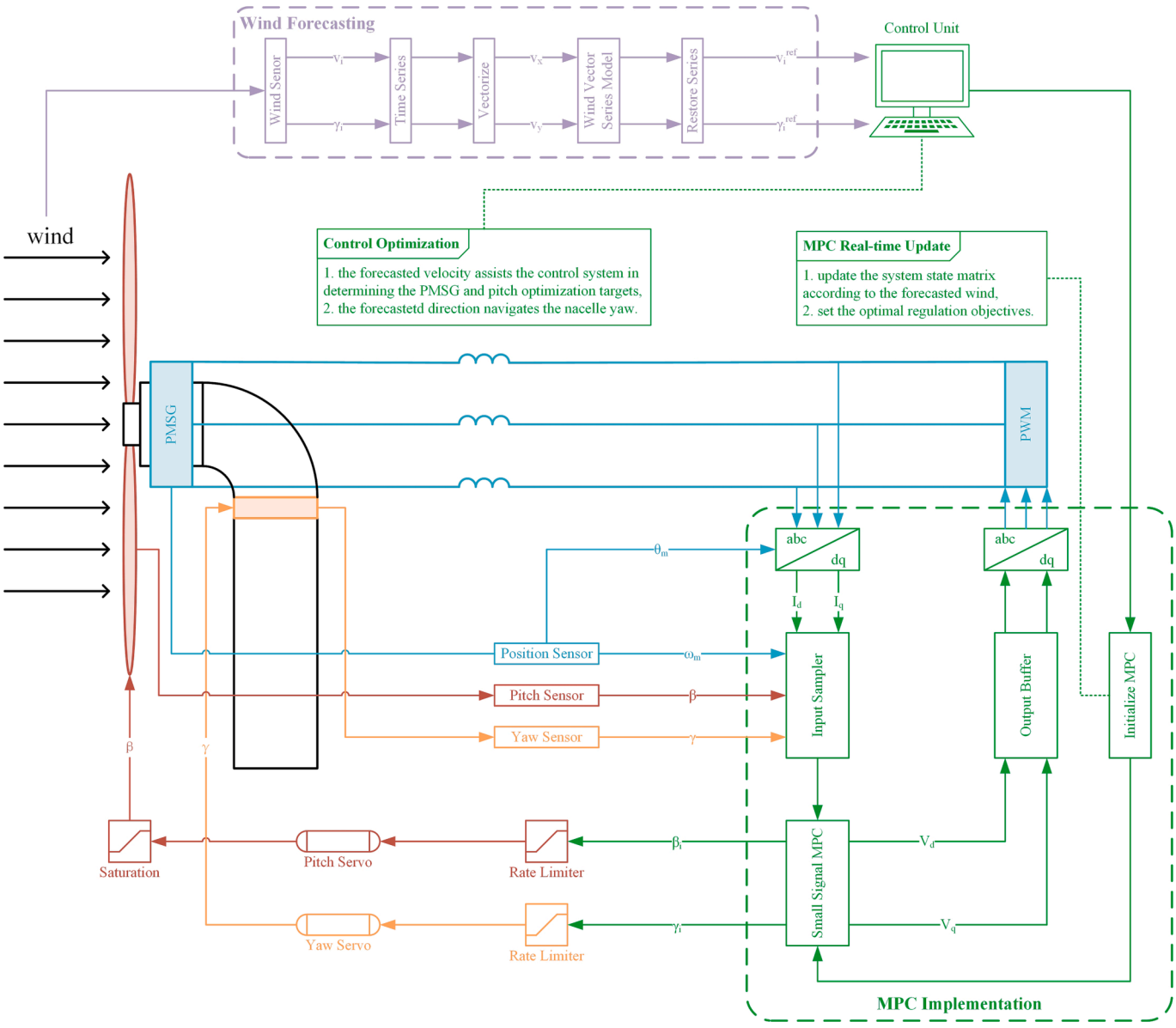

Fig. 14. The schematic diagram of the wind forecasting-based MPC.

(*continued*)

Algorithm 1. Control input reference optimisation

6. **if** the target is less than the maximum $P_d^{max} > P_t$:
7. increase β_{ref} until $\mathscr{J}\left(\beta_{ref}\right) = \min\left(\text{abs}\left(\mathscr{M}|_{P_d} - P_t\right)\right)$
8. update $P_d^{ref} \leftarrow \left[v_i,\ \omega_d^{ref},\ \beta_{ref}\right]$
9. **else**
10. accept the maximum solution $P_d^{ref} = P_d^{max}$
11. linearize torque sensitivities at selected speed and pitch $(\frac{\partial Q_d}{\partial \omega_d}, \frac{\partial Q_d}{\partial \beta})$
12. return $\omega_d^{ref}, \beta_{ref}, P_d^{ref}, \frac{\partial Q_d}{\partial \omega_d}, \frac{\partial Q_d}{\partial \beta}$

Fig. 12 examples **steps 1 ~ 10** of **Algorithm 1** at a wind speed of 10 m/s. Firstly, **Algorithm 1** moves the rotor speed on the zero-pitch curve, determining the optimal rotor speed with the optimal TSR. Secondly, **Algorithm 1** gradually increases the pitch angle to reach the desired output.

Fig. 13 provides an example of the PRPT running **Algorithm 1**. The 100 % output curve is the same as the MPPT. Compared with the MPPT, the PRPT provides a flexible power range to ensure constant power over different wind velocities.

4. Turbine control

The control objective of the 3-DOF IEA 15-MW is to regulate the nacelle, shaft, and blade to the optimal reference of yaw, speed, and pitch derived from **section 3.5**. When the system works at the nominated operational point, it should capture and deliver the needed power. This section introduces a fully coupled system model and establishes the corresponding MPC optimisation.

4.1. Control design

The control objects include a PMSG that balances torque for stable rotation and absorbs captured wind power, a pitch servo that adjusts pitch angle to affect aerodynamics and a yaw servo that navigates the rotor of blades to face wind flow. Fig. 14 visualises the control flow from wind forecasting to terminal devices. The wind forecasting with

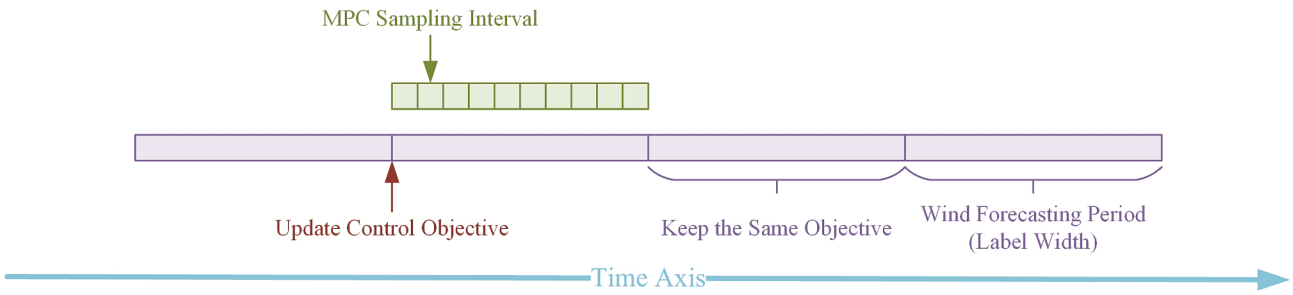

Fig. 15. The time definition of the forecasting-based MPC.

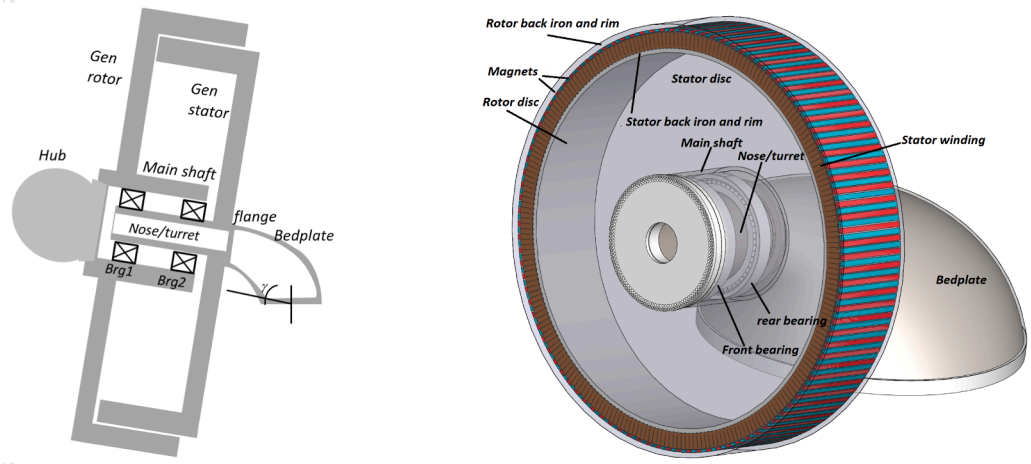

a) a sketch of the PMSG layout b) a CAD model of the nacelle layout

Fig. 16. The direct-drive PMSG of the IEA 10-MW.

operation optimisation calculates the optimal rotation, pitch, and yaw. The pitch and yaw references are direct control inputs, but the speed reference needs to be the voltage and current signal of the PMSG. Meanwhile, the control system initializes the predictive model (i.e., system matrix) inside the MPC according to the working point. After setting the control objective and system matrix of the PMSG and servos, the MPC is responsible for changing states and eliminating errors caused by either system noises or external wind stochastics.

Since wind forecasting and control have different response frequencies, Fig. 15 explains their working period on the time axis. First, each wind forecasting period, i.e., the label width (30-s) in Fig. 7, circularly updates the control objective (speed, pitch, and yaw references) according to the received wind prediction (**Eqs. (16)(17)**). The control objective remains the same until the next forecast. The MPC sampling interval (or working period) is much faster than the forecasting period, in which the MPC samples the system state and solves the QP optimisation. A shorter interval is not always the best because the processing unit cannot compute the QP solution immediately, so a higher sampling frequency is meaningless in accuracy. The MPC interval is 1 ms, considering a trade-off between fast response and computational cost.

4.2. System modelling

The fundamental DOF of WECS is the main shaft rotation that delivers received mechanical power to the generator side [34]. The rotor control, i.e., speed control, targets maintaining system rotation at desired speeds by regulating the generator output torque [20]. Since the IEA 15-MW couples the generator rotor and the main shaft, a stiff shaft model [35] (**Eq. (23)**) can depict the system rotation with aerodynamic input Q_d and PMSG load Q_e. Table 1 lists the shaft parameters.

$$J_t\dot{\omega}_d = Q_d - Q_e - D_t\omega_d \tag{23}$$

The essence of the PMSG control is to change the voltage condition and affect the electromagnetic torque on the terminal side of the main shaft [36]. The PMSG relies on permanent magnets to achieve magnetizing, thus not requiring any external excitation current [32]. Joining the nacelle structure, the direct-drive PMSG, a type of radial flux outer-rotor generator, yields a simple and compact layout shown in Fig. 16 [5]. The PMSG model, including output torque [36], decouples into fractious d and q-axis components through the virtual stator winding, as given in **Eqs. (24)(25)(26)** [32].

$$V_d = R_s I_d - \omega_e L_q I_q + L_d \dot{I}_{dr} \tag{24}$$

$$V_q = R_s I_q + \omega_e L_d I_d + L_q \dot{I}_q + \omega_e \psi_f \tag{25}$$

$$Q_e = \frac{3p}{k_g}\left(\left(L_d - L_q\right)I_d - \psi_f\right)I_q = -\frac{3p}{k_g}\psi_f I_q \tag{26}$$

where ω_e is the synchronous speed varying with the rotor speed. Table 1 lists the PMSG parameters. **Eqs. (24)(25)** reflect the state transition of PMSG under the controllable stator voltage signals. **Eq. (26)** explicitly calculates the generator torque from the rotor current. From the generator's perspective, the speed control is equivalent to the torque control [32].

Most pitching [37] and yawing [38] systems in wind energy refer to servo systems that track input reference. The pitch and yaw controllers behave as a model of the dynamic system with amplitude and output limitations, which the first-order system can represent [39]. With time constants τ_β and τ_γ, **Eqs. (27)(28)** describe the response of the pitch β and yaw γ servos. It notes that three blade pitch servos of the IEA 15-MW

are under collective pitch control and have an identical response [40].

$$\dot{\beta} = \frac{1}{\tau_\beta}(\beta_i - \beta) \tag{27}$$

$$\dot{\gamma} = \frac{1}{\tau_\gamma}(\gamma_i - \gamma) \tag{28}$$

where β_i and γ_i are the input reference of the pitch and yaw servos. Table 1 lists the servo parameters. One characteristic of pitch [33] and yaw [38] is that both have movement constraints due to servo load capacity. The pitch servo has double-side position boundaries that normally satisfy $\in (0^\circ,\ 90^\circ)$. The yaw system can navigate at any angle around the compass circle.

To parse system dynamic variation and give explicit transition representation, a small signal analysis [41] on **Eqs. (23)~(28)** derives an incremental form of the response of the shaft rotation, PMSG, pitch angle, and yaw position, as indicated in **Eq. (29)**.

$$\begin{cases} \Delta\dot{\omega}_d = \dfrac{1}{J_T}(\Delta Q_d - \Delta Q_e - D_t\Delta\omega_d) \\ \Delta Q_d = \dfrac{\partial Q_d}{\partial \omega_d}\Delta\omega_d + \dfrac{\partial Q_d}{\partial \beta}\Delta\beta \\ \Delta Q_e = -\dfrac{3p}{k_g}\psi_f \Delta I_q \\ \Delta\dot{I}_d = -\dfrac{R_s}{L_d}\Delta I_d + \dfrac{\omega_e L_q}{L_d}\Delta I_{qr} + \dfrac{\Delta V_d}{L_d} \\ \Delta\dot{I}_q = -\dfrac{\omega_e L_d}{L_q}\Delta I_d - \dfrac{R_s}{L_q}\Delta I_{qr} + \dfrac{\Delta V_q}{L_q} \\ \Delta\dot{\beta} = \dfrac{1}{\tau_\beta}(\Delta\beta_i - \Delta\beta) \\ \Delta\dot{\gamma} = \dfrac{1}{\tau_\gamma}(\Delta\gamma_i - \Delta\gamma) \end{cases} \tag{29}$$

Compared with **Eq. (23)**, the equation set **Eq. (29)** introduces an item of linearized shaft response under speed and pitch variation. Substituting the aerodynamic input deviation and the PMSG torque response into the rotor speed equation yields a linearized rotation governing equation **Eq. (30)**.

$$\Delta\dot{\omega}_d = \frac{1}{J_T}\left(\left(\frac{\partial Q_d}{\partial \omega_d} - D_t\right)\Delta\omega_d + \frac{3p}{k_g}\psi_f\Delta I_q + \frac{\partial Q_d}{\partial \beta}\Delta\beta\right) \tag{30}$$

where $\frac{\partial Q_d}{\partial \omega_d}$ and $\frac{\partial Q_d}{\partial \beta}$ are estimated torque sensitivities [23] from the operation optimiser.

After **Eq. (30)** simplifies **Eq. (29)**, a state space **Eq. (31)** around the working point estimates the system state Δx under the influence of the control vector Δu.

$$\Delta\dot{x} = A\Delta x + B\Delta u \tag{31}$$

$$\Delta x = \left[\Delta\omega_d,\ \Delta I_d,\ \Delta I_q,\ \Delta\beta,\ \Delta\gamma\right]^T \tag{32}$$

$$\Delta u = \left[\Delta V_d,\ \Delta V_q,\ \Delta\beta_i,\ \Delta\gamma_i\right]^T \tag{33}$$

$$A = \begin{bmatrix} \frac{1}{J_t}\frac{\partial Q_d}{\partial \omega_d} - \frac{D_t}{J_t} & 0 & \frac{3p\psi_f}{J_t k_g} & \frac{1}{J_t}\frac{\partial Q_d}{\partial \beta} & 0 \\ 0 & -\frac{R_s}{L_d} & \frac{\omega_e L_q}{L_d} & 0 & 0 \\ 0 & -\frac{\omega_e L_d}{L_q} & -\frac{R_s}{L_q} & 0 & 0 \\ 0 & 0 & 0 & -\frac{1}{\tau_\beta} & 0 \\ 0 & 0 & 0 & 0 & -\frac{1}{\tau_\gamma} \end{bmatrix} \tag{34}$$

$$B = \begin{bmatrix} 0 & 0 & 0 & 0 \\ \frac{1}{L_d} & 0 & 0 & 0 \\ 0 & \frac{1}{L_q} & 0 & 0 \\ 0 & 0 & \frac{1}{\tau_\beta} & 0 \\ 0 & 0 & 0 & \frac{1}{\tau_\gamma} \end{bmatrix} \tag{35}$$

The PMSG currents, pitch angle, and yaw angles are actuator states, so integral items [42] are included in the system state to enhance control steady-state accuracy. It results in updating the state space to **Eqs. (36) (37)(38)** with the same input vector.

$$\Delta x = \left[\Delta_0,\ \Delta_1,\ \Delta_2,\ \Delta_3,\ \Delta_4,\ \int\Delta_1,\ \int\Delta_2,\ \int\Delta_3,\ \int\Delta_4\right]^T \tag{36}$$

$$A = \begin{bmatrix} a_{00} & 0 & a_{02} & a_{03} & 0 & 0 & 0 & 0 & 0 \\ 0 & a_{11} & a_{12} & 0 & 0 & 0 & 0 & 0 & 0 \\ 0 & a_{21} & a_{22} & 0 & 0 & 0 & 0 & 0 & 0 \\ 0 & 0 & 0 & a_{33} & 0 & 0 & 0 & 0 & 0 \\ 0 & 0 & 0 & 0 & a_{44} & 0 & 0 & 0 & 0 \\ 0 & 1 & 0 & 0 & 0 & 0 & 0 & 0 & 0 \\ 0 & 0 & 1 & 0 & 0 & 0 & 0 & 0 & 0 \\ 0 & 0 & 0 & 1 & 0 & 0 & 0 & 0 & 0 \\ 0 & 0 & 0 & 0 & 1 & 0 & 0 & 0 & 0 \end{bmatrix} \tag{37}$$

$$B = \begin{bmatrix} 0 & 0 & 0 & 0 \\ b_{10} & 0 & 0 & 0 \\ 0 & b_{21} & 0 & 0 \\ 0 & 0 & b_{32} & 0 \\ 0 & 0 & 0 & b_{43} \\ 0 & 0 & 0 & 0 \\ 0 & 0 & 0 & 0 \\ 0 & 0 & 0 & 0 \\ 0 & 0 & 0 & 0 \end{bmatrix} \tag{38}$$

4.3. Model predictive control

The MPC has various applications in the WECS. For example, Lin et al. considered mechanical load and power optimisation in the MPC design [43]. Wakui et al. tried to use the MPC to stabilize the power output and platform motion of a floating WT system [3]. Yao et al. introduced distributed MPCs at a wind farm level to suppress tower fatigue loads [41]. Current MPCs almost adopt standard MPC libraries that employ the ADMM solver [41] to solve the MPC optimisation. However, recent QP solvers are much faster than the original ADMM since they accelerate computing for the sparse matrix. Besides, most MPCs in the WECS only deal with the 2-DOF system (speed and pitch), and some simplify the generator model as a linear torque model. Firstly, the proposed MPC fully couples necessary devices (PMSG, pitch and yaw servos) for the 3-DOF control. Secondly, the MPC optimisation is formalized to a standard sparse-matrix problem so that a general-

purpose QP solver is available to use.

A native objective of the receding horizontal predictive control is to reach desired system states with minimum control input, which yields a quadratic optimisation objective of the MPC [43]. **Eq. (39)** represents the optimisation objective of a small signal MPC, which takes N steps prediction to measure the deviation about the regulation objective x_{obj} and the control cost [3].

$$\mathscr{J} = \min\left(\sum_{k=0}^{N} \Delta x_k^T Q \Delta x_k + \sum_{k=0}^{N-1} \Delta u_k^T R \Delta u_k\right) \tag{39}$$

$$s.t. \begin{cases} \Delta x_{k+1} = A_d \Delta x_k + B_d \Delta u_k \\ x_{min} \le x_{ref} + \Delta x_k \le x_{max} \\ u_{min} \le u_{ref} + u_k \le u_{max} \\ \Delta x_0 = \Delta \overline{x} \end{cases} \tag{40}$$

$$Q = \mathrm{diag}(q_0,\ q_1,\ q_2,\ q_3,\ q_4,\ q_5,\ q_6,\ q_7,\ q_8) \tag{41}$$

$$R = \mathrm{diag}(r_0,\ r_1,\ r_2,\ r_3) \tag{42}$$

where x_k and u_k are the discrete state and input variables at a time step, $A_d = e^{At_s}$ and $B_d = \int_0^{t_s} e^{A(t_s-t)}dt \bullet B$ discrete the system state, and $\overline{x}$ is the sampled state. Q and R are semi-definite and positive definite weights for scaling state deviation and input cost [43]. The IEA 15-MW adopts a horizontal length of 20.

Eqs. (43)(44) configure the weighting matrics of the IEA 15-MW. This weighting assumes a higher priority for the rotor speed. Besides, the PMSG has a lower regulation intensity due to the high sensitivity of the electromagnetic torque. In contrast, each control input has the same priority.

$$Q = \mathrm{diag}(1000,\ 0.01,\ 0.01,\ 1,\ 1,\ 0.001,\ 0.001,\ 0.001,\ 0.001) \tag{43}$$

$$R = \mathrm{diag}(1,\ 1,\ 1,\ 1) \tag{44}$$

The MPC optimisation is a typical QP problem that can be solved using active-set, interior-point or augmented-Lagrangian methods [44]. This study applies a native QP solver-based approach to find the MPC solution. Let $\mathscr{P}$ and $\mathscr{q}$ define symmetric and linear costs, **Eq. (45)** expresses a standard QP problem [45] considering equality constraints and bound constraints.

$$\mathscr{J} = \min\left(\frac{1}{2}\mathscr{x}^T \mathscr{P} \mathscr{x} + \mathscr{q}^T \mathscr{x}\right) \tag{45}$$

$$s.t. \begin{cases} Ax = b \\ l \le x \le u \end{cases} \tag{46}$$

Owing to the computational efficiency of the sparse matrix, a state-constrained method [46] transforms **Eq. (39)** into a form of **Eq. (45)**. Assuming a predictive horizon has n_x state variables and n_u input variables, **Eqs. (47)~(53)** update the MPC optimisation. It is worth mentioning that the state objective of a small signal MPC is zero, which accounts for a zero sequence of **Eq. (49)**.

$$\mathscr{x} = [\Delta x_0, \cdots,\ \Delta x_N,\ \Delta u_0, \cdots,\ \Delta u_{N-1}]^T \tag{47}$$

$$\mathscr{P} = \begin{bmatrix} \overbrace{\begin{matrix} Q & \cdots & 0_{n_x} \\ \vdots & \ddots & \vdots \\ 0_{n_x} & \cdots & Q \end{matrix}}^{N+1} & \cdots & 0_{n_x \times n_u} \\ 0_{n_u \times n_x} & \cdots & \underbrace{\begin{matrix} R & \cdots & 0_{n_u} \\ \vdots & \ddots & \vdots \\ 0_{n_u} & \cdots & R \end{matrix}}_{N} \end{bmatrix} \tag{48}$$

$$\mathscr{q} = \left[\underbrace{0_{n_x} \cdots}_{N+1},\ \underbrace{0_{n_u} \cdots}_{N}\right]^T \tag{49}$$

$$\mathscr{A} = \begin{bmatrix} \underbrace{\begin{matrix} -I_{n_x} & 0_{n_x} & \cdots & 0_{n_x} \\ A_d & -I_{n_x} & \ddots & \vdots \\ \vdots & \ddots & \ddots & 0_{n_x} \\ 0_{n_x} & \cdots & A_d & -I_{n_x} \end{matrix}}_{(N+1)\times(N+1)} & \underbrace{\begin{matrix} 0_{n_u} & 0_{n_u} & \cdots & 0_{n_u} \\ B_d & 0 & \ddots & \vdots \\ \vdots & \ddots & \ddots & 0_{n_u} \\ 0_{n_u} & \cdots & B_d & 0_{n_u} \end{matrix}}_{(N+1)\times N} \end{bmatrix} \tag{50}$$

$$\mathscr{l} = \left[-\Delta x_0,\ \underbrace{0_{n_x} \cdots}_{N}\right]^T \tag{51}$$

$$\mathscr{\ell} = \left[\underbrace{x_{min} - x_{ref} \cdots}_{N+1},\ \underbrace{u_{min} - u_{ref} \cdots}_{N}\right]^T \tag{52}$$

$$\mathscr{u} = \left[\underbrace{x_{max} - x_{ref} \cdots}_{N+1},\ \underbrace{u_{max} - u_{ref} \cdots}_{N}\right]^T \tag{53}$$

where Δx_0 is the sampled small-signal state. Although the MPC suggests n_u control input sequences, only the first control input Δu_0 takes effect on the next horizon. The ProxyQP selected as the QP solver is an augmented Lagrangian method that consists of a preprocessing procedure, an initialization for primal and dual candidates, and a cold restart strategy [45].

4.4. Control loop

Only pitch and yaw are straightforward objectives in the 3-DOF system, and rotor rotation needs to be a signal that the PMSG can accept. **Eqs. (24)(25)** indicates that the PMSG adjusts the stator voltage according to the output current error to produce a proper electric torque for torque equilibrium and stable rotation. Under the given rotor speed ω_d^{ref} and estimated power capture P_d^{ref} from **Algorithm 1**, **Eqs. (54)(55)** calculates the current reference $(I_d^{ref},\ I_q^{ref})$ of PMSG [47].

$$I_d^{ref} = -\frac{Q_s^{ref}}{3V_g} \tag{54}$$

$$I_q^{ref} = -\frac{P_s^{ref}}{3V_g} \tag{55}$$

$$P_s^{ref} \approx k_g P_d^{ref} \tag{56}$$

$$Q_s^{ref} = K_{pf} P_s^{ref} \tag{57}$$

$$V_g = p \bullet \psi_f \omega_d^{ref} \tag{58}$$

where $K_{pf} = \tan(\arccos(pf))$ is the power factor coefficient, $pf = 1$ and $K_{pf} = 0$ for the regular operation of the PMSG. The PMSG motor model accounts for the negative sign of the output current. **Eq. (58)** indicates the phase voltage has a linear proportion relationship with the rotor speed. Besides, neglecting time-derivative items in **Eqs. (24)(25)** leads to the voltage reference $(V_d^{ref},\ V_q^{ref})$.

When a PMSG runs in actual wind conditions, there will be a power gap between the model power and the actual output due to model accuracy and wind fluctuation. Therefore, the system probably drifts away from the given rotor speed. A speed compensator f_s (**Eqs. (60)**) corrects the q-axis current I_q^{sig} according to the speed error $\Delta\omega_d$.

$$I_q^{sig} = (1 + f_s) \bullet I_q^{ref} \tag{59}$$

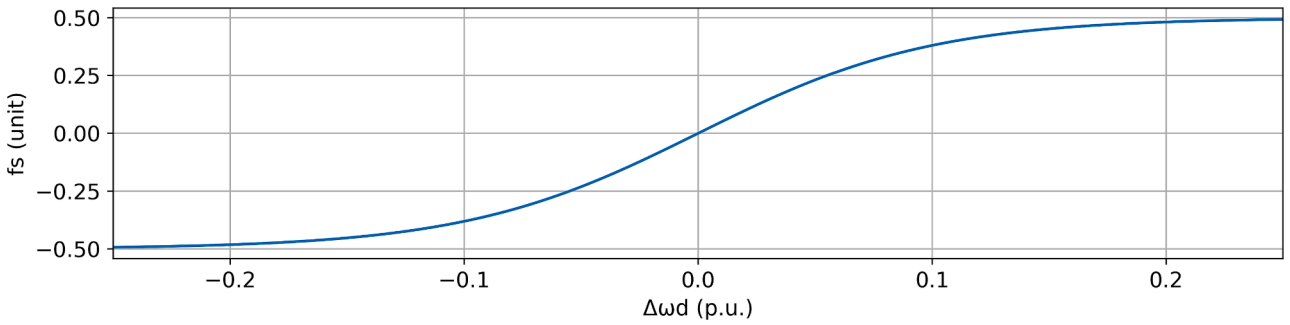

Fig. 17. The S-curve for speed error compensation.

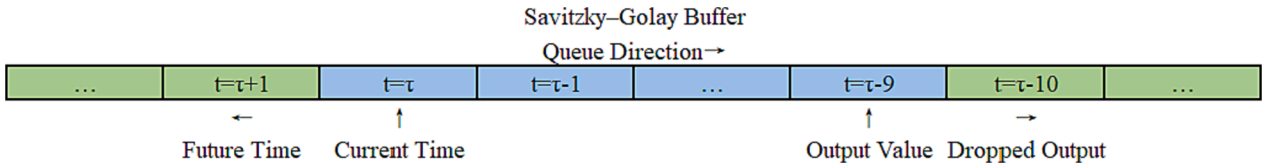

Fig. 18. The moving buffer of the Savizky-Golay filter.

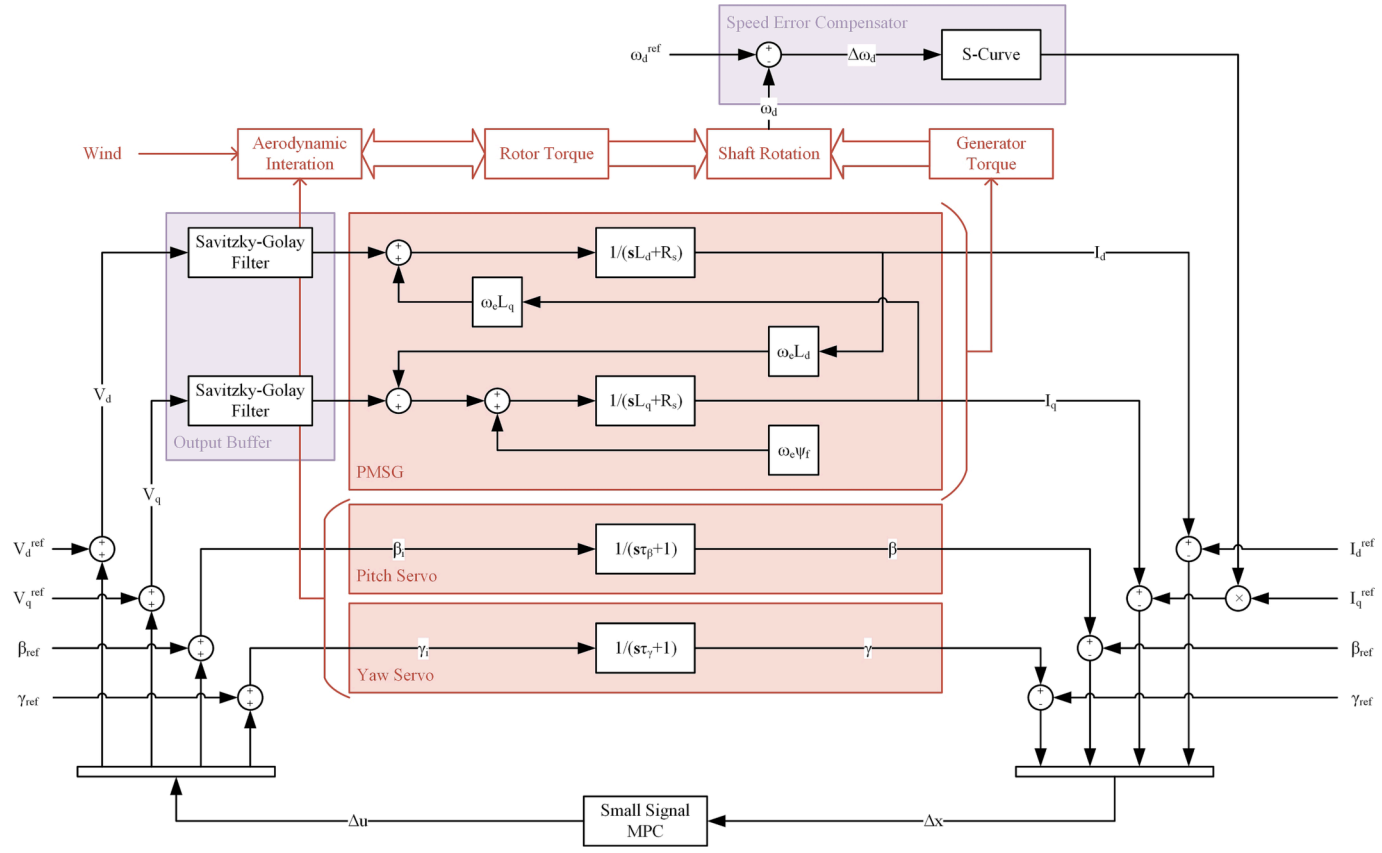

Fig. 19. The feedback loop of the small signal MPC controlling the PMSG, pitch servo, and yaw servo.

$$f_s(\Delta\omega_d) = L_{sf} \bullet \left(\frac{2}{1+\exp(-K_{sf} \bullet \Delta\omega_d)} - 1 \right) \tag{60}$$

$$\Delta\omega_d = \frac{\omega_d - \omega_d^{ref}}{\omega_d^{ref}} \tag{61}$$

where f_s has a S-shape symmetrical at the origin. K_{sf} affects the slope at the origin and L_{sf} limits the compensation range. Fig. 17 draws f_s with $K_{sf} = 20$ and $L_{sf} = 0.5$. The compensator reduces the PMSG generation to raise the rotor speed below the desired speed and increases the generator torque to slow down for overspeeding.

Since wind variation and operation adjustment result in power fluctuation, two Savizky-Golay filters [48] cascade the MPC voltage output as a buffer to reduce oscillation. The Savizky-Golay filter is a kind of least-squares polynomial smoothing (**Eq. (62)**) that minimizes the

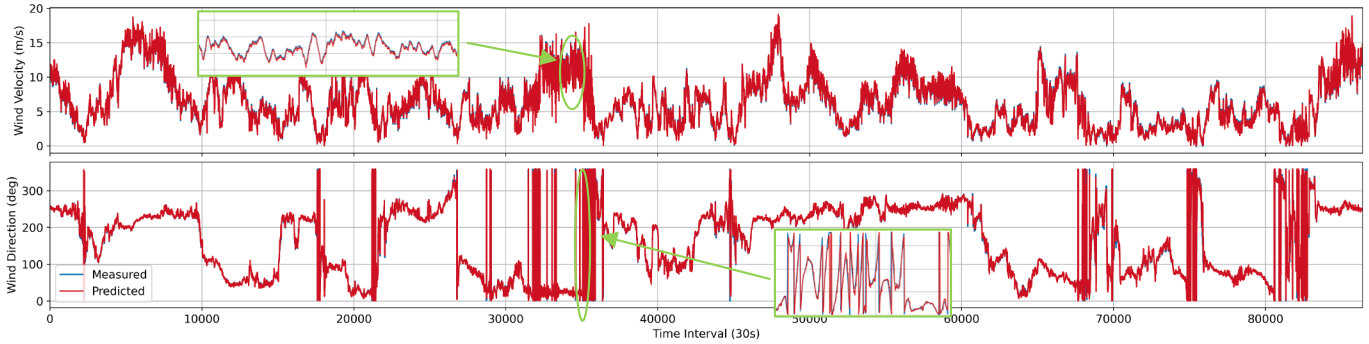

a) the DNN

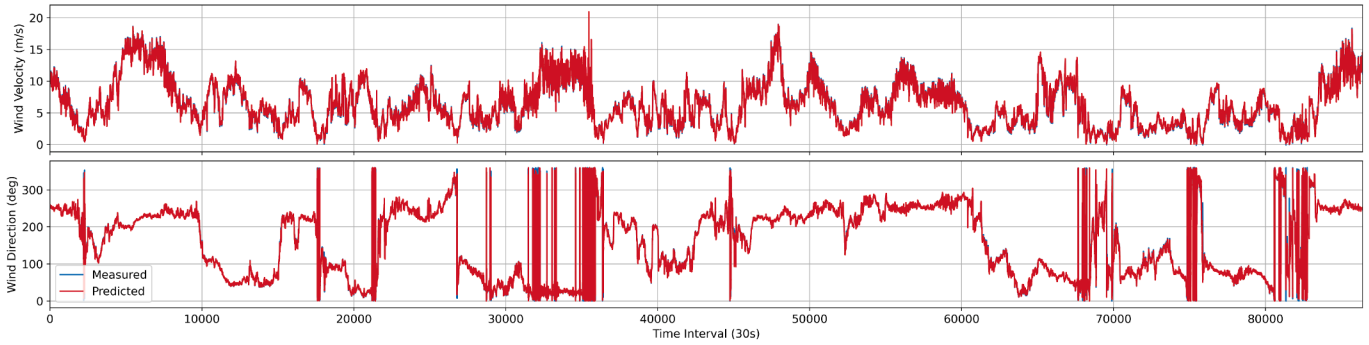

b) the CNN

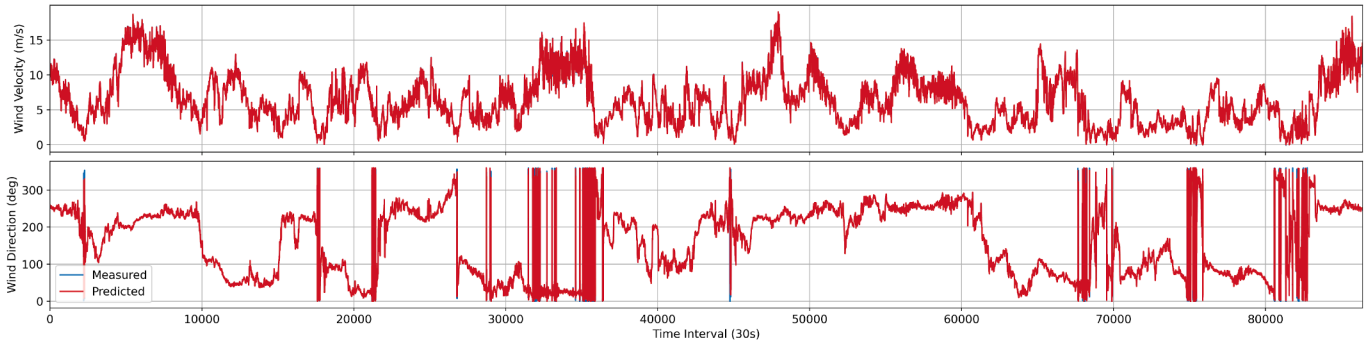

c) the LSTM

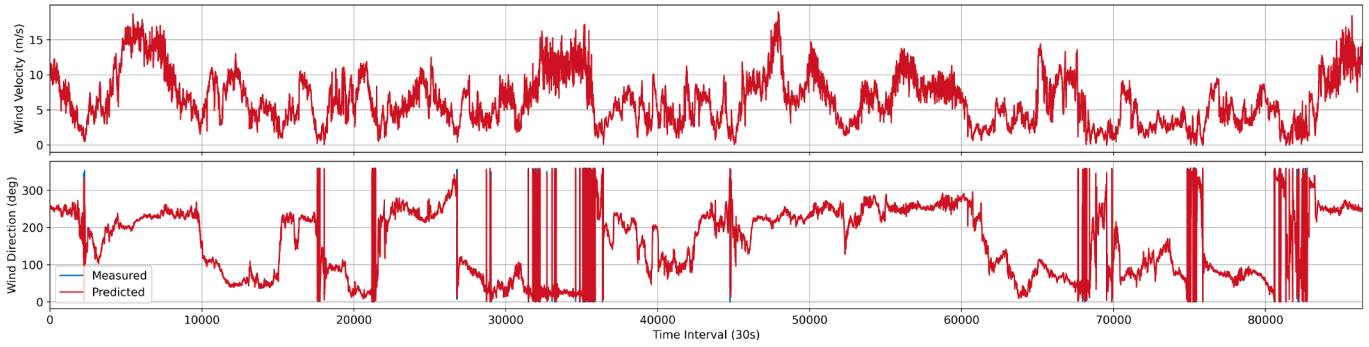

d) the CNN-LSTM

Fig. 20. An example of wind series forecasting on one-month data.

Table 7
The statistical result of model predictions over 30 tests.

			Mean	Std.	Min.	25 %	50 %	75 %	Max.
MLPN	v_i(m/s)	R2	0.9969	0.0006	0.9952	0.9966	0.9970	0.9974	0.9978
		MAE	0.0696	0.0359	0.0278	0.0417	0.0610	0.0881	0.1778
		RMSE	0.1961	0.0188	0.1644	0.1816	0.1945	0.2051	0.2453
	θ_v(°)	R2	0.9969	0.0009	0.9938	0.9966	0.9970	0.9976	0.9979
		MAE	0.6272	0.3784	0.2467	0.3976	0.5345	0.7547	1.9528
		RMSE	4.8753	0.6284	4.0581	4.3771	4.8631	5.1295	6.9666
CNN	v_i(m/s)	R2	0.9977	0.0004	0.9968	0.9976	0.9977	0.9980	0.9982
		MAE	0.0494	0.0196	0.0286	0.0336	0.0434	0.0579	0.0999
		RMSE	0.1688	0.0133	0.1500	0.1597	0.1675	0.1725	0.1994
	θ_v(°)	R2	0.9974	0.0004	0.9961	0.9973	0.9975	0.9977	0.9980
		MAE	0.4468	0.1859	0.2593	0.3214	0.4188	0.4891	1.1263
		RMSE	4.4847	0.3353	3.9698	4.2824	4.4312	4.6185	5.5511
LSTM	v_i(m/s)	R2	0.9979	0.0002	0.9975	0.9978	0.9979	0.9980	0.9984
		MAE	0.0394	0.0096	0.0277	0.0329	0.0371	0.0443	0.0635
		RMSE	0.1624	0.0074	0.1434	0.1589	0.1628	0.1675	0.1755
	θ_v(°)	R2	0.9973	0.0003	0.9966	0.9971	0.9972	0.9974	0.9979
		MAE	0.3577	0.0767	0.2567	0.3084	0.3410	0.3991	0.5361
		RMSE	4.6320	0.2287	4.0804	4.4830	4.6702	4.7458	5.1869
CNN-LSTM	v_i(m/s)	R2	0.9977	0.0002	0.9971	0.9976	0.9977	0.9978	0.9982
		MAE	0.0451	0.0133	0.0270	0.0352	0.0433	0.0499	0.0762
		RMSE	0.1689	0.0086	0.1518	0.1653	0.1684	0.1714	0.1890
	θ_v(°)	R2	0.9974	0.0003	0.9970	0.9972	0.9974	0.9976	0.9980
		MAE	0.4187	0.0830	0.2929	0.3558	0.4259	0.4792	0.5757
		RMSE	4.4910	0.2498	3.9378	4.3335	4.5116	4.6770	4.8721

mean-squared approximation error $\mathscr{E}_N$ for the group of $2M+1$ input samples $x[n]$ centred on $n=0$ [48].

$$\mathscr{E}_N = \sum_{n=-M}^{M} (p(n) - x[n])^2 = \sum_{n=-M}^{M} \left(\sum_{k=0}^{N} \alpha_k n^k - x[n] \right)^2 \tag{62}$$

where $p(n) = \sum_{k=0}^{N} \alpha_k n^k$ is a polynomial process to be decribed. The Savizky-Golay window and order are 5 and 2 for the 15-MW PMSG.

Fig. 18 explains the movement of applying the Savizky-Golay filter on a voltage sequence. The current output value is a smoothed value before 9 buffer samples. This moving buffer lags the control voltage acting on the PMSG. More buffer samples improve smoothness, but a long buffer ruins stability due to control lag. The trade-off between smoothing and control response accounts for a buffer size 10.

Therefore, an entire MPC control loop includes the system reference forecasted by the wind model, the dynamic system, the QP optimisation, the PMSG voltage-current control, and the voltage buffer, as shown in Fig. 19.

5. Case study

The case study will first examine and compare the forecasting accuracy of four wind models (DNN, CNN, LSTM, and CNN-LSTM). After model verification, a simulation will test the 3-DOF MPC of the IEA 15-MW with and without wind forecasting.

5.1. Wind forecasting

Wind forecasting is a core component in the proposed control system of the IEA 15-MW that provides wind velocity to regulate output power and wind direction to navigate yaw angle. Fig. 20 displays the compass wind forecasted by four time-series models. Given a 30-s prediction length, there will be 86,400 predictions for a 30-day wind series. According to the figures, predicted wind speeds align with actual velocities and achieve high accuracy. Predicted yaw angles often match wind directions and keep track of rapid fluctuations.

Table 7 trains each model 30 times and summarises the evaluation indexes in **section 3.4**. Four models achieve an average R^2 of over 0.996 in wind speed and direction, indicating the wind modelling frame of the compass-vector transformation and vector series model is feasible and reliable. However, there are some noticeable model differences. Firstly, the MLPN has the worst direction prediction, considering a max MAE of 1.95° and a max RMSE of 6.97°. Therefore, a conventional stacked-layer network is weaker than a network containing feature extraction or recurrent structure. The CNN enhances the direction accuracy compared with the MLPN, but its stability is slightly worse than the LSTM and CNN-LSTM. The reason is that the CNN primarily relies on the dense layer to learn features extracted by the convolution. Therefore, a model with a recurrent base is more suitable for wind vector series.

Considering most metric distributions, the LSTM and CNN-LSTM have similar performance and surpass the MLPN and CNN. Nevertheless, the LSTM has tiny advantages except for the RMSE of direction, which manifests that the encoder-decoder design has no promotion. The CNN-LSTM theoretically can increase the learning efficiency of complex and diverse features, but the wind vector has only two projection features. Therefore, the encoder-decoder cannot further improve the LSTM. In conclusion, the LSTM has accurate predictions, stable training results, and economic parameters. The following control simulation will use the LSTM as the wind forecasting model.

5.2. Synthesis control

Since the WT operation depends on the wind reference in each forecasting period, this section will investigate the MPC of WECS with or without forecasting for high and medium wind intensities. There will be four cases:

i. 100% power production at a wind speed range of 14.5~16 m/s,
ii. 50% power production with the above series,
iii. 50% power production at a range of 9.4~9.8 m/s,
iv. 25% power production with the above series.

Since **case i** satisfied the rated output condition of the conventional MPPT, this case also includes a control design derived from the NREL baseline [49]. The baseline control integrates a direct-driven PMSG speed-torque control [33], a perturbation observation-based MPPT [32], a collective pitch control [50], and a pitch-gain scheduling [51]. The non-forecasted and baseline simulations average the input wind series as the most frequent observation [19]. **Case i** compares and discusses the performance and reliability of the proposed MPC, and **cases (ii, iii, iv)** examine the effects of wind forecasting and power stability.

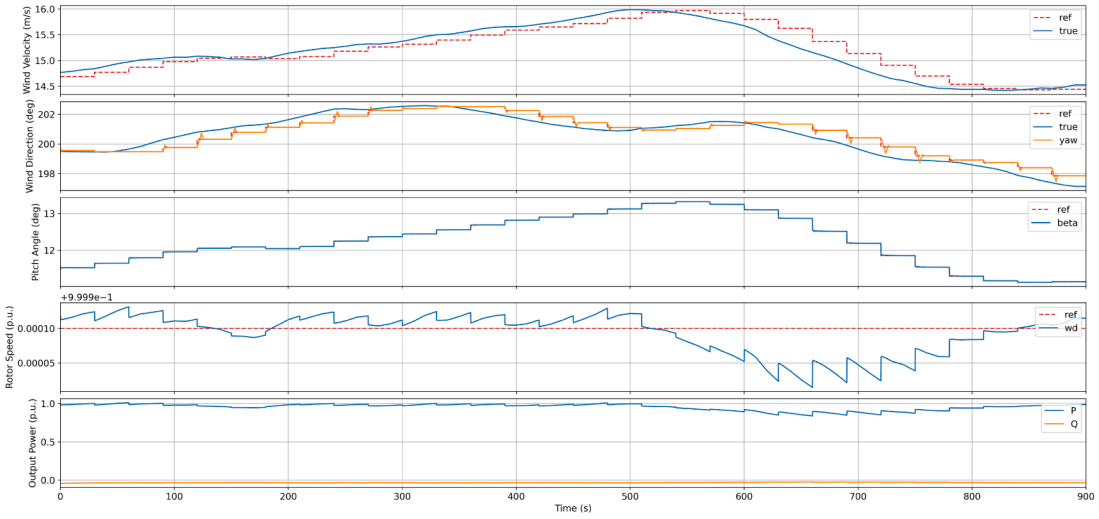

a) baseline

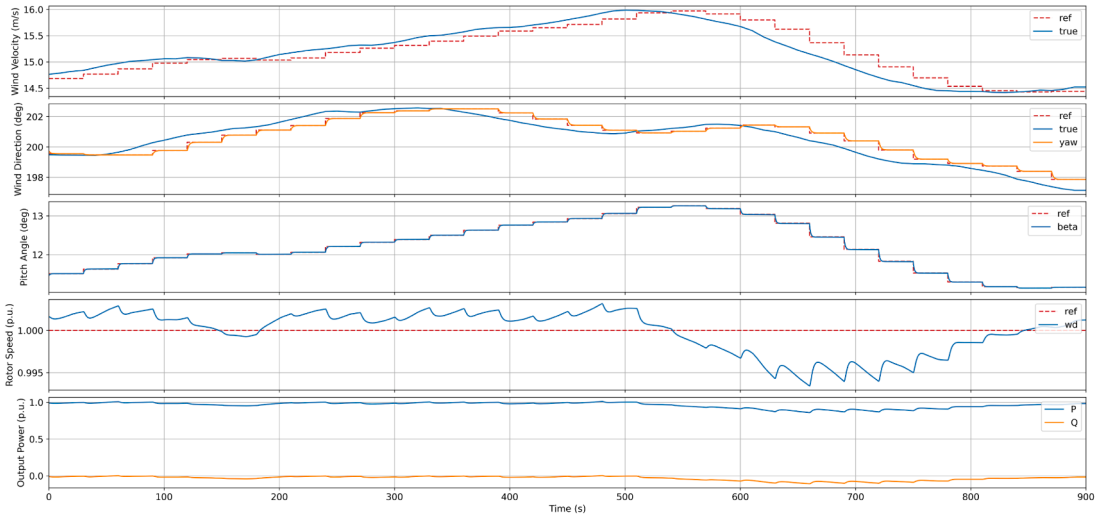

b) non-forecasted

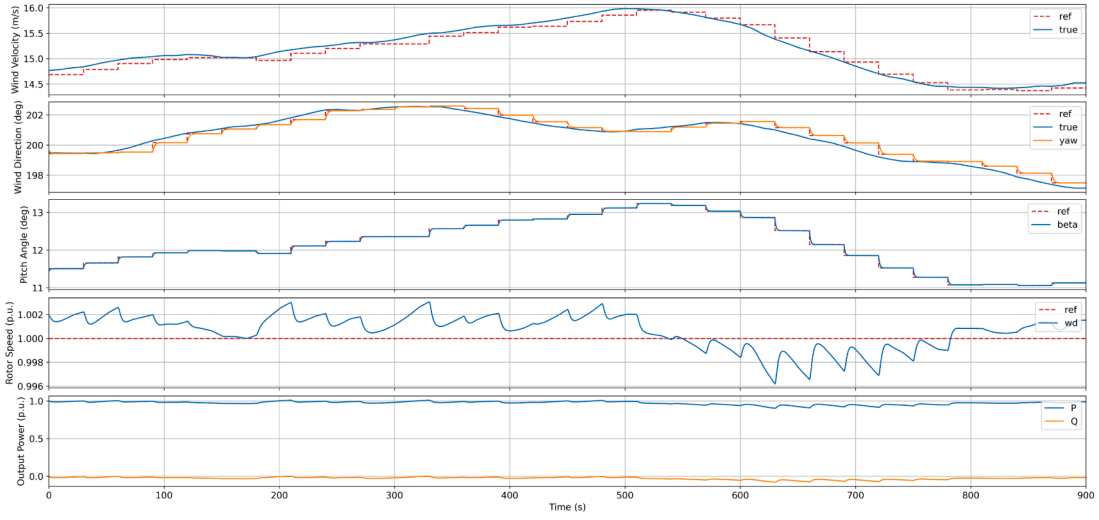

c) forecasted

Fig. 21. 100% power production for case i.

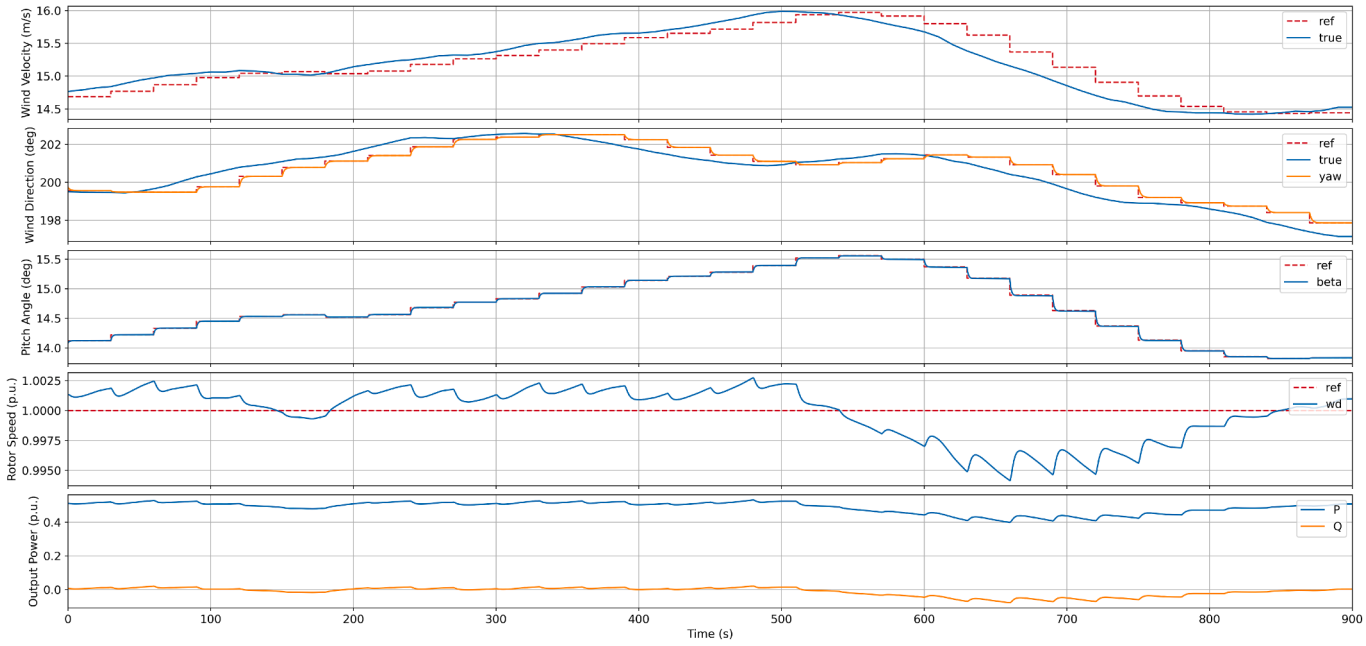

a) non-forecasted

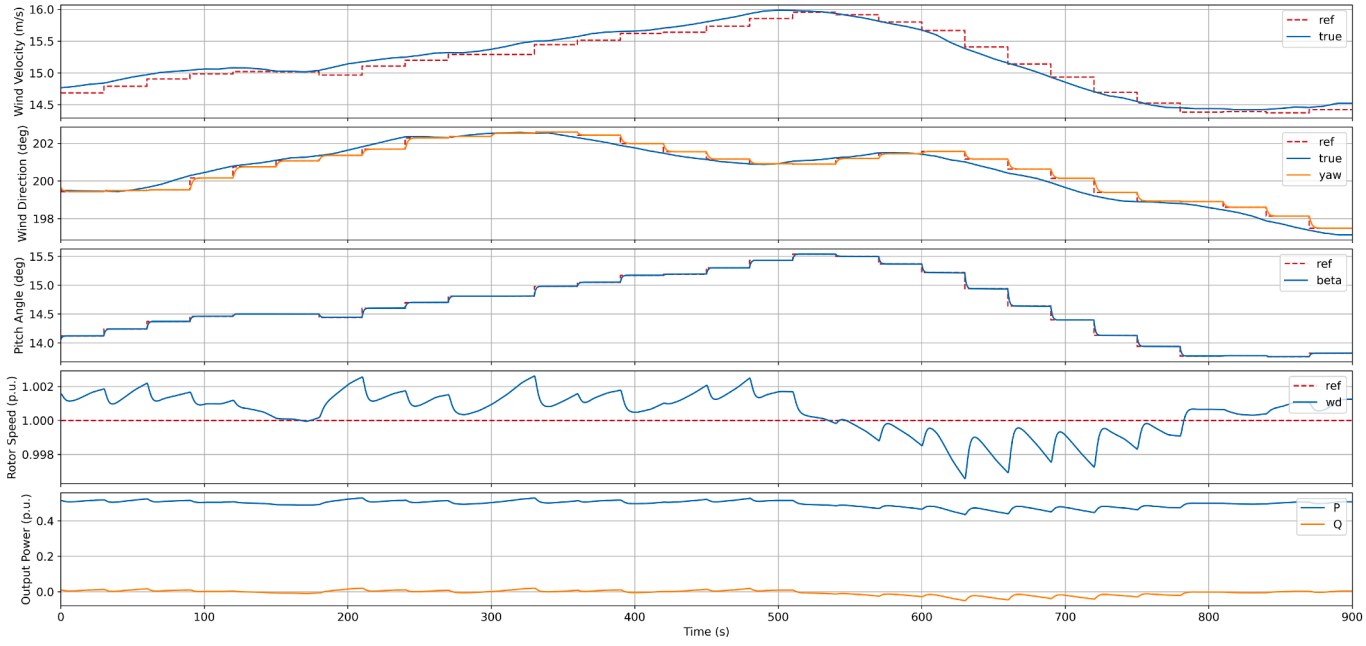

b) forecasted

Fig. 22. 50% power production for case ii.

5.2.1. High-velocity scenario

Wind speed over 10.2 m/s can ensure sufficient wind capture for the rated power production, to which the high-velocity scenario of 14.5~16 m/s corresponds. Fig. 21 runs the full-load operation of the IEA 15-MW under three control configurations. The baseline and non-forecasted cases share the same wind data processing, but their rotation and production differ significantly. Firstly, the baseline regards the rotor rotation as the dominant control objective, which accounts for fewer rotation fluctuations (less than 0.0001 p.u.). On the contrary, the MPC balances the multiple objectives of **Eq. (36)**, which allows moderate speed variation for better power quality. Therefore, the MPC power is intuitively smoother than the baseline, especially when updating wind references.

The forecasted control has a more stable rotor speed and power output than the non-forecasted. The rotor speed of the forecasted control distributes from 0.996 to 1.003 p.u. However, the non-forecasted fluctuates from 0.993 p.u. to 1.003 p.u., and its fluctuations look more aggressive. As one of the most critical stability indexes, the rotor speed reflects the capability of suppressing incoming wind uncertainties of a control design. Since the wind forecasting model provides a reliable wind estimation, the control unit updates an accurate MPC objective. Thus, control results are close to expectations. When examining velocity and direction predictions, the forecasting model behaves like sampling future winds with the zero-hold method. In contrast, the non-forecasted method cannot reach such accuracy. For example, the region of 570~780-s has an apparent gap between wind reference and actual

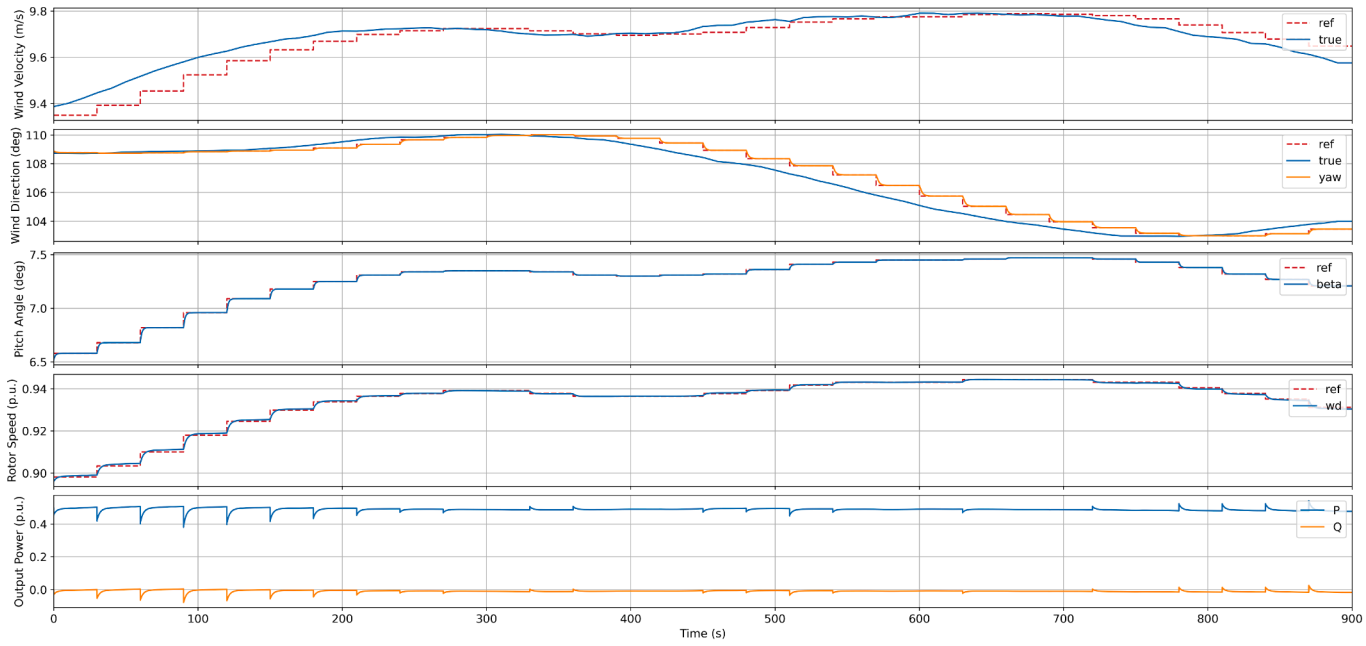

a) non-forecasted

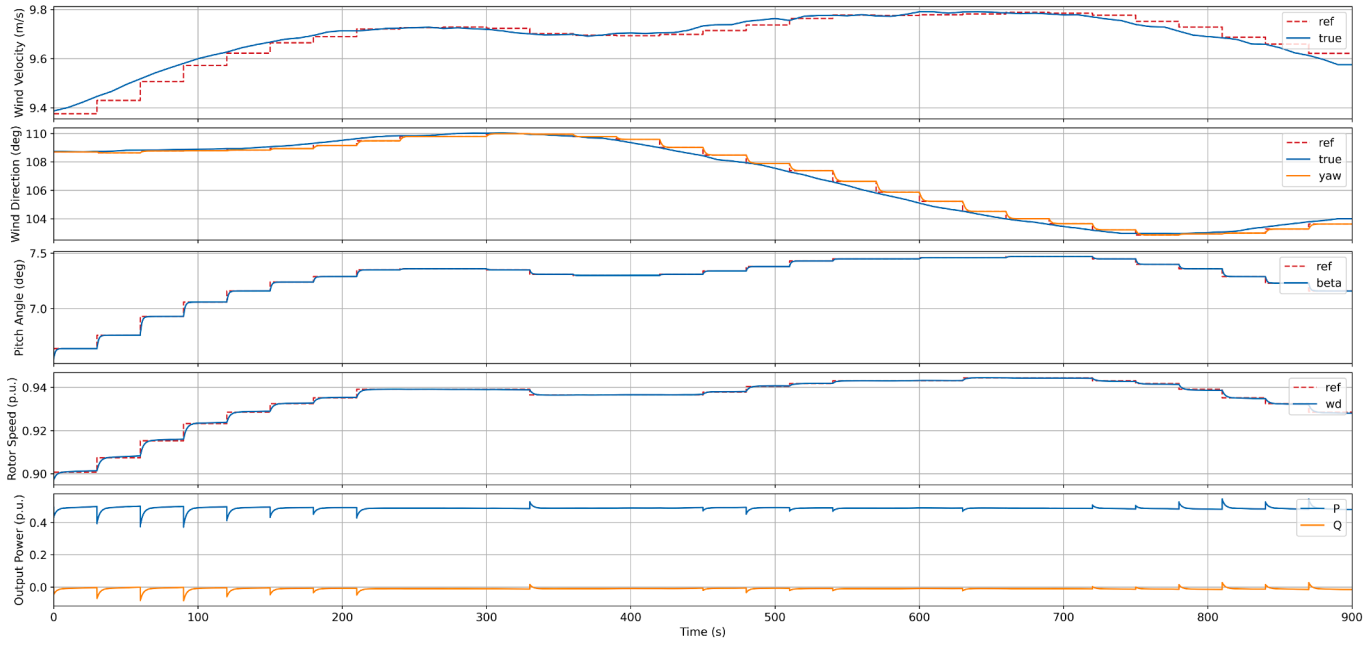

b) forecasted

Fig. 23. 50% power production for case iii.

wind.

When lowering the power target to 50%, both rotor speeds in Fig. 22 fluctuate less because a lower target naturally reduces the aerodynamic load. Thus, the MPC can more easily handle fluctuation. Like the 100% case, the forecasted control performs better in stabilizing the rotor speed. In terms of output, the lowest output of the non-forecasted almost touches 0.4 p.u., farther than the forecasted.

5.2.2. *Medium-velocity scenario*

The control performance at medium wind speeds is more practical due to the concentration shown in Fig. 6 and Table 2. Regarding wind references in Fig. 23, forecasted speeds and directions still closely track upcoming winds. However, non-forecasted winds have obvious mismatches, e.g., wind speed before 210 s and wind direction in 420∼720 s. Due to the variable speed operation in Region ii, there are conspicuous power spikes before 210 s and after 750 s. It is hard for a WT to eliminate these spikes because rotation response and power smoothness are contradictory. A fast rotor regulation requires the PMSG to change torque immediately, resulting in power spikes. It is helpful to place a circuit filter or energy storage [52] to absorb these spikes.

Fig. 24 decreases the output target to 25% for the same wind series in Fig. 23. Although the non-forecasted wind reference drifts away from measurement, the rotor speed and output power do not exhibit noteworthy differences compared to the high-velocity cases. The internal linearization of MPC handles modest aerodynamic variation well, so wind forecasting has less effect in the medium-velocity cases.

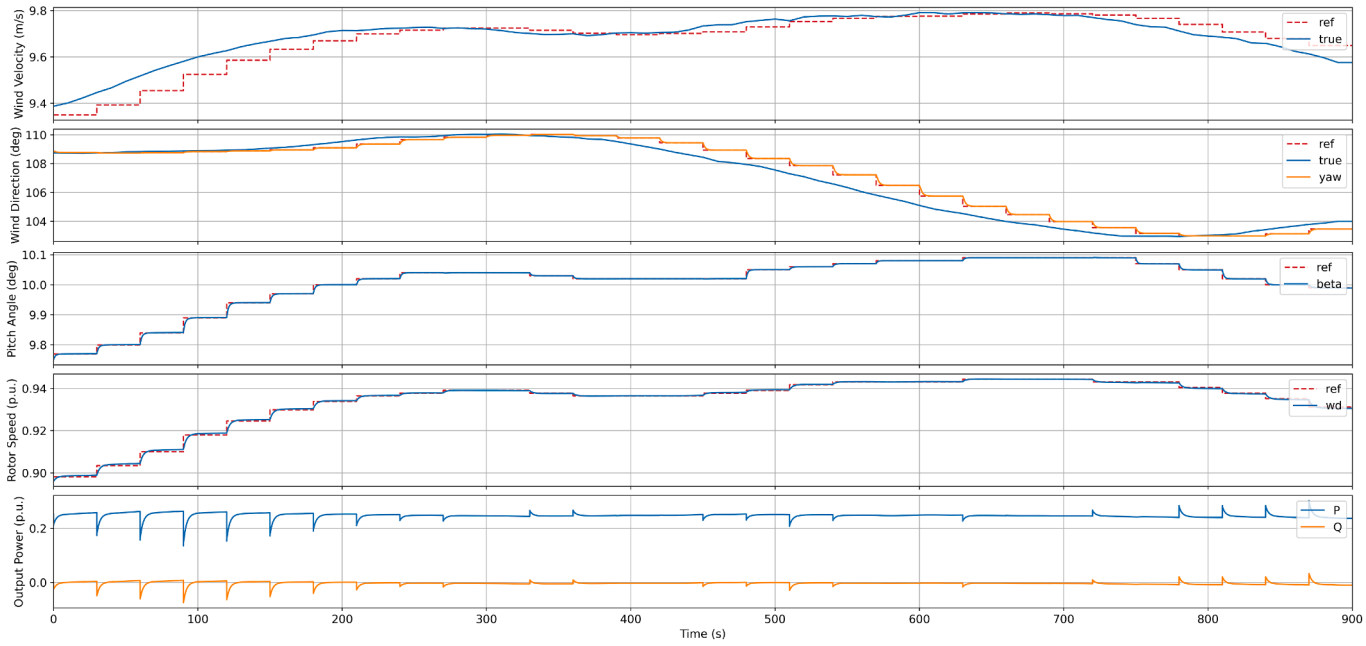

a) non-forecasted

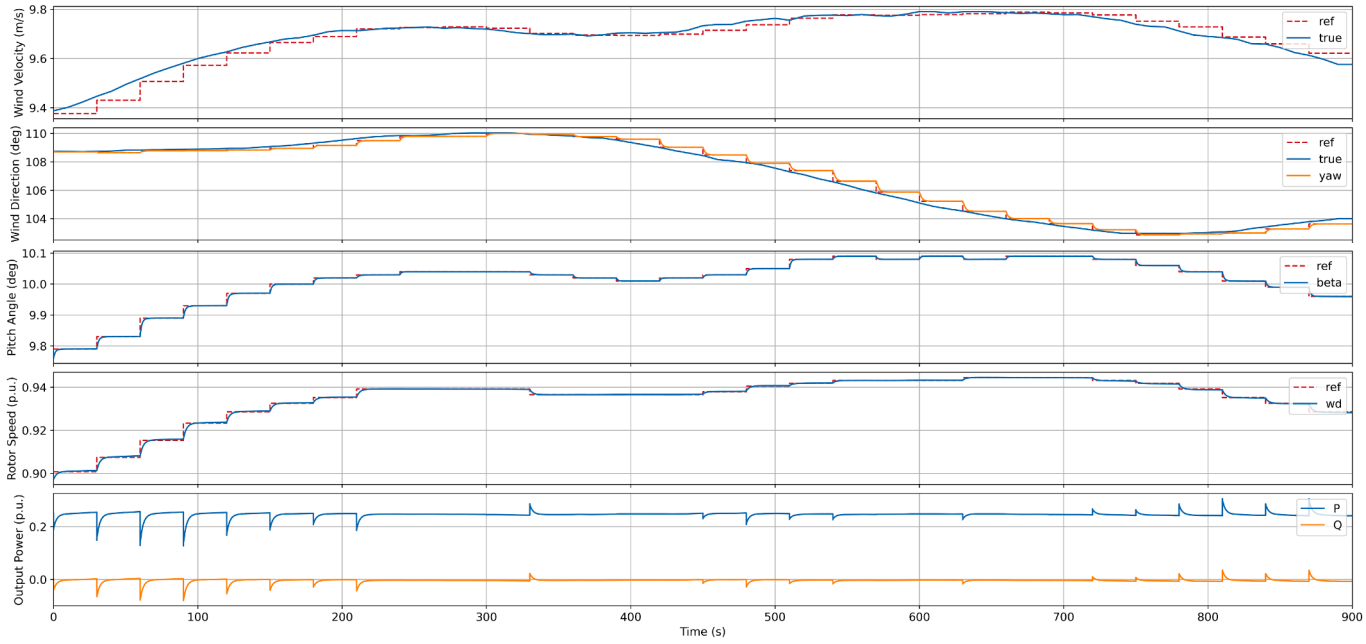

b) forecasted

Fig. 24. 25% power production for case iv.

Table 8 summarises statistical results about rotor speed and output power in Fig. 21∼Fig. 24. Firstly, the baseline ensures a stable rotation with the minimum speed deviation, which gives rise to more output fluctuation for fast speed response. Compared with the baseline, the MPC can improve an average output of 0.007 p.u., reduce 7% of power variation, and alleviate 12% of output peak-to-peak, contributing to a higher power quality. With wind forecasting, the power production has a mean promotion of 0.01 p.u., and the rotation and output fluctuation remarkably reduces at least 44% in **cases i and ii**. However, **cases iii and iv** only diminish about 10% of rotation fluctuation but improve nothing for power quality. Wind forecasting is not helpful to low-load scenarios because the MPC robustness is enough to compensate for wind error. In conclusion, the wind forecasting-based MPC has advantages in rotation stability and effectively improves power quality at heavy loads.

6. Conclusion

This study proposes a wind forecasting-based MPC that uses wind prediction to optimise system configuration and integrates the generator and servo control for constant output. The proposed wind forecasting achieves direction series prediction on the foundation of the conventional wind speed model. Meanwhile, the forecasting section comprehensively investigates feature analysis, compass-vector transformation, series windowing, learning-shaping structure, and four deep-learning networks. Besides, wind forecasting integrates a novel operation

Table 8
The statistical summary of the above simulations.

Wind velocity	Output target	Control		Mean	Std.	Min.	Max.
High	100 %	baseline	ω (p.u.)	0.99999	0.00003	0.99991	1.00003
	case i	Fig. 21 **a)**	P (p.u.)	0.95566	0.04164	0.83801	1.01133
		non-forecasted	ω (p.u.)	0.99992	0.00248	0.99343	1.00319
		Fig. 21 **b)**	P (p.u.)	0.96279	0.03859	0.86092	1.01363
		forecasted	ω (p.u.)	1.00064	0.00136	0.99619	1.00307
		Fig. 21 **c)**	P (p.u.)	0.97389	0.02139	0.90360	1.01125
	50 %	non-forecasted	ω (p.u.)	0.99986	0.00217	0.99415	1.00274
	case ii	Fig. 22 **a)**	P (p.u.)	0.48802	0.03365	0.39819	0.53187
		forecasted	ω (p.u.)	1.00049	0.00119	0.99658	1.00262
		Fig. 22 **b)**	P (p.u.)	0.49771	0.01868	0.43543	0.53038
Medium	50 %	non-forecasted	ω (p.u.)	0.93437	0.01163	0.89610	0.94449
	case iii	Fig. 23 **a)**	P (p.u.)	0.48971	0.00887	0.38035	0.54343
		forecasted	ω (p.u.)	0.93492	0.01050	0.89728	0.94451
		Fig. 23 **b)**	P (p.u.)	0.48876	0.00870	0.37154	0.54659
	25 %	non-forecasted	ω (p.u.)	0.93438	0.01169	0.89600	0.94451
	case iv	Fig. 24 **a)**	P (p.u.)	0.24718	0.00865	0.13496	0.30242
		forecasted	ω (p.u.)	0.93494	0.01053	0.89720	0.94452
		Fig. 24 **b)**	P (p.u.)	0.24644	0.00878	0.12720	0.30625

optimisation to interpret wind series prediction to the system working point. The model evaluation indicates that the convolutional or recurrent structure surpasses the simple layer stack, and the recurrent layer is more efficient, which accounts for a model ranking (LSTM≥CNN-LSTM>CNN>DNN). The average accuracy of the LSTM reaches a r-square of at least 0.9973. This trustworthy performance can help the MPC perceive wind stochastic variation in advance.

As the key of WECS, the MPC, enhanced by wind forecasting, coordinates the PMSG, pitch servo, and yaw servo for a 3-DOF regulation of speed, pitch, and yaw. Proven by the baseline comparison, the MPC with the state-of-the-art QP solver and sparse-matrix QP construction has a persuasive control performance of multiple objectives. Also, four wind and output scenarios verify that wind forecasting strengthens rotation stability and power smoothness. In particular, wind forecasting can lower about 44% of rotor speed and output power oscillation at high wind speed. Integrating wind series forecasting and 3-DOF turbine control reinforces wind energy controllability and promotes wind power stability.

CRediT authorship contribution statement

Tenghui Li: Conceptualization, Data curation, Formal analysis, Investigation, Methodology, Resources, Software, Visualization, Writing – original draft. **Jin Yang:** Investigation, Resources, Supervision, Validation, Writing – review & editing. **Anastasia Ioannou:** Supervision, Validation, Writing – review & editing.

Declaration of competing interest

The authors declare that they have no known competing financial interests or personal relationships that could have appeared to influence the work reported in this paper.

Data availability

Data will be made available on request.

References

[1] Chen Y, et al. 2-D regional short-term wind speed forecast based on CNN-LSTM deep learning model. Energ Conver Manage 2021;244. https://doi.org/10.1016/j.enconman.2021.114451.

[2] Tavakol Aghaei V, et al. Energy optimization of wind turbines via a neural control policy based on reinforcement learning Markov chain Monte Carlo algorithm. Appl Energy, vol. 341, 2023, doi: 10.1016/j.apenergy.2023.121108.

[3] Wakui T, Nagamura A, Yokoyama R. Stabilization of power output and platform motion of a floating offshore wind turbine-generator system using model predictive control based on previewed disturbances. Renew Energy 2021;173:105–27. https://doi.org/10.1016/j.renene.2021.03.112.

[4] Sun S, Liu Y, Li Q, Wang T, Chu F. Short-term multi-step wind power forecasting based on spatio-temporal correlations and transformer neural networks. Energ Conver Manage 2023;283. https://doi.org/10.1016/j.enconman.2023.116916.

[5] Gaertner E, et al. IEA wind TCP task 37: definition of the IEA 15-megawatt offshore reference wind turbine. National Renewable Energy Lab (NREL), Golden, CO (United States) 2020.

[6] Song D, et al. New perspectives on maximum wind energy extraction of variable-speed wind turbines using previewed wind speeds. Energ Conver Manage 2020;206. https://doi.org/10.1016/j.enconman.2020.112496.

[7] Wen S, Li Y, Su Y. A new hybrid model for power forecasting of a wind farm using spatial–temporal correlations. Renew Energy 2022;198:155–68. https://doi.org/10.1016/j.renene.2022.08.044.

[8] Wang Y, Zou R, Liu F, Zhang L, Liu Q. A review of wind speed and wind power forecasting with deep neural networks. Appl Energy 2021;304. https://doi.org/10.1016/j.apenergy.2021.117766.

[9] Jaseena KU, Kovoor BC. Decomposition-based hybrid wind speed forecasting model using deep bidirectional LSTM networks. Energ Conver Manage 2021;234. https://doi.org/10.1016/j.enconman.2021.113944.

[10] Richmond M, Sobey A, Pandit R, Kolios A. Stochastic assessment of aerodynamics within offshore wind farms based on machine-learning. Renew Energy 2020;161:650–61. https://doi.org/10.1016/j.renene.2020.07.083.

[11] Liu J, Huang X, Li Q, Chen Z, Liu G, Tai Y. Hourly stepwise forecasting for solar irradiance using integrated hybrid models CNN-LSTM-MLP combined with error correction and VMD. Energ Conver Manage 2023;280. https://doi.org/10.1016/j.enconman.2023.116804.

[12] Neshat M, et al. A deep learning-based evolutionary model for short-term wind speed forecasting: A case study of the Lillgrund offshore wind farm. Energ Conver Manage 2021;236. https://doi.org/10.1016/j.enconman.2021.114002.

[13] Ahmed R, Sreeram V, Togneri R, Datta A, Arif MD. Computationally expedient Photovoltaic power Forecasting: A LSTM ensemble method augmented with adaptive weighting and data segmentation technique. Energ Conver Manage 2022;258. https://doi.org/10.1016/j.enconman.2022.115563.

[14] Xiang L, Liu J, Yang X, Hu A, Su H. Ultra-short term wind power prediction applying a novel model named SATCN-LSTM. Energ Conver Manage 2022;252. https://doi.org/10.1016/j.enconman.2021.115036.

[15] Ewees AA, Al-qaness MAA, Abualigah L, Elaziz MA. HBO-LSTM: Optimized long short term memory with heap-based optimizer for wind power forecasting. Energ Conver Manage 2022;268. https://doi.org/10.1016/j.enconman.2022.116022.

[16] Agga A, Abbou A, Labbadi M, Houm YE, Ou Ali IH. CNN-LSTM: An efficient hybrid deep learning architecture for predicting short-term photovoltaic power production. Electric Power Systems Research, vol. 208, 2022, doi: 10.1016/j.epsr.2022.107908.

[17] Fu W, Fu Y, Li B, Zhang H, Zhang X, Liu J. A compound framework incorporating improved outlier detection and correction, VMD, weight-based stacked generalization with enhanced DESMA for multi-step short-term wind speed forecasting. Appl Energy 2023;348. https://doi.org/10.1016/j.apenergy.2023.121587.

[18] Neshat M, et al. Wind turbine power output prediction using a new hybrid neuro-evolutionary method. Energy 2021;229. https://doi.org/10.1016/j.energy.2021.120617.

[19] Manwell JF, McGowan JG, Rogers AL. Wind Energy Explained: Theory. Design and Application: Second Edition. John Wiley & Sons; 2010.

[20] Liu J, Meng H, Hu Y, Lin Z, Wang W. A novel MPPT method for enhancing energy conversion efficiency taking power smoothing into account. Energ Conver Manage 2015;101:738–48. https://doi.org/10.1016/j.enconman.2015.06.005.

[21] Gambier A, Meng F. Control system design for a 20 MW reference wind turbine. In *2019 IEEE Conference on Control Technology and Applications (CCTA)*, 2019: IEEE, pp. 258-263.
[22] Kelkoul B, Boumediene A. Stability analysis and study between classical sliding mode control (SMC) and super twisting algorithm (STA) for doubly fed induction generator (DFIG) under wind turbine. Energy 2021;214. https://doi.org/10.1016/j.energy.2020.118871.
[23] Li T, Liu X, Lin Z, Yang J, Ioannou A. A linear quadratic regulator with integral action of wind turbine based on aerodynamics forecasting for variable power production. Renew Energy 2023. https://doi.org/10.1016/j.renene.2023.119605.
[24] Srinivasa Sudharsan G, Natarajan K, Rahul SG, Kumar A. Active power control in horizontal axis wind turbine considering the fatigue structural load parameter using psuedo adaptive- model predictive control scheme. Sustainable Energy Technologies and Assessments, vol. 57, 2023, doi: 10.1016/j.seta.2023.103166.
[25] Bortolotti P, et al. IEA Wind TCP Task 37: Systems engineering in wind energy-WP2. 1 Reference wind turbines. National Renewable Energy Lab (NREL), Golden, CO (United States) 2019.
[26] Zhang C, Zhou J, Li C, Fu W, Peng T. A compound structure of ELM based on feature selection and parameter optimization using hybrid backtracking search algorithm for wind speed forecasting. Energ Conver Manage 2017;143:360–76. https://doi.org/10.1016/j.enconman.2017.04.007.
[27] Liu L, Wang J, Li J, Wei L. An online transfer learning model for wind turbine power prediction based on spatial feature construction and system-wide update. Appl Energy 2023;340. https://doi.org/10.1016/j.apenergy.2023.121049.
[28] Zhang Y, Li Y, Zhang G. Short-term wind power forecasting approach based on Seq2Seq model using NWP data. Energy 2020;213. https://doi.org/10.1016/j.energy.2020.118371.
[29] TensorFlow. "Time series forecasting." https://www.tensorflow.org/tutorials/structured_data/time_series (accessed Aug, 2023).
[30] Li T, Liu X, Lin Z, Morrison R. Ensemble offshore Wind Turbine Power Curve modelling – An integration of Isolation Forest, fast Radial Basis Function Neural Network, and metaheuristic algorithm. Energy 2022;239. https://doi.org/10.1016/j.energy.2021.122340.
[31] Kisvari A, Lin Z, Liu X. Wind power forecasting – A data-driven method along with gated recurrent neural network. Renew Energy 2021;163:1895–909. https://doi.org/10.1016/j.renene.2020.10.119.
[32] Chen J, Yao W, Zhang C-K, Ren Y, Jiang L. Design of robust MPPT controller for grid-connected PMSG-Based wind turbine via perturbation observation based nonlinear adaptive control. Renew Energy 2019;134:478–95. https://doi.org/10.1016/j.renene.2018.11.048.
[33] Pan L, Wang X. Variable pitch control on direct-driven PMSG for offshore wind turbine using Repetitive-TS fuzzy PID control. Renew Energy 2020;159:221–37. https://doi.org/10.1016/j.renene.2020.05.093.
[34] Song D, et al. A novel wind speed estimator-integrated pitch control method for wind turbines with global-power regulation. Energy 2017;138:816–30. https://doi.org/10.1016/j.energy.2017.07.033.
[35] Song D, et al. Maximum wind energy extraction of large-scale wind turbines using nonlinear model predictive control via Yin-Yang grey wolf optimization algorithm. Energy 2021;221. https://doi.org/10.1016/j.energy.2021.119866.
[36] Zholtayev D, Rubagotti M, Do TD. Adaptive super-twisting sliding mode control for maximum power point tracking of PMSG-based wind energy conversion systems. Renew Energy 2022;183:877–89. https://doi.org/10.1016/j.renene.2021.11.055.
[37] Ren Y, Li L, Brindley J, Jiang L. Nonlinear PI control for variable pitch wind turbine. Control Eng Pract 2016;50:84–94. https://doi.org/10.1016/j.conengprac.2016.02.004.
[38] Song D, et al. Deep optimization of model predictive control performance for wind turbine yaw system based on intelligent fuzzy deduction. Expert Syst Appl 2023;221. https://doi.org/10.1016/j.eswa.2023.119705.
[39] Zhao X, Lin Z, Fu B, Gong S. Research on frequency control method for micro-grid with a hybrid approach of FFR-OPPT and pitch angle of wind turbine. Int J Electr Power Energy Syst 2021;127. https://doi.org/10.1016/j.ijepes.2020.106670.
[40] Hur S, Leithead WE. Collective control strategy for a cluster of stall-regulated offshore wind turbines. Renew Energy 2016;85:1260–70. https://doi.org/10.1016/j.renene.2015.07.087.
[41] Yao Q, Hu Y, Zhao T, Guan Y, Luo Z, Liu J. Fatigue load suppression during active power control process in wind farm using dynamic-local-reference DMPC. Renew Energy 2022;183:423–34. https://doi.org/10.1016/j.renene.2021.10.069.
[42] Hong Q-R, Chan P-I, Sou W-K, Gong C, Lam C-S. Linear quadratic regulator optimal control with integral action (LQRIC) for LC-coupling hybrid active power filter. Appl Sci 2022;12(19):pp. https://doi.org/10.3390/app12199772.
[43] Lin Z, Chen Z, Liu J, Wu Q. Coordinated mechanical loads and power optimization of wind energy conversion systems with variable-weight model predictive control strategy. Appl Energy 2019;236:307–17. https://doi.org/10.1016/j.apenergy.2018.11.089.
[44] Caron S. Optimality conditions and numerical tolerances in QP solvers. https://github.com/qpsolvers/qpsolvers_benchmark (accessed Nov, 2023).
[45] Bambade A, El-Kazdadi S, Taylor A, Carpentier J. Prox-qp: Yet another quadratic programming solver for robotics and beyond. RSS 2022-Robotics. Science and Systems; 2022.
[46] Stellato B, Banjac G, Goulart P, Bemporad A, Boyd S. OSQP: an operator splitting solver for quadratic programs. Math Program Comput 2020;12(4):637–72. https://doi.org/10.1007/s12532-020-00179-2.
[47] Prince MKK, Arif MT, Haque ME, Gargoom A, Oo AMT. Design and implementation of finite control set MPC with an LCL filter for grid-tied PMSG based wind turbine. Int J Electr Power Energy Syst 2023;152. https://doi.org/10.1016/j.ijepes.2023.109197.
[48] Schafer R. What Is a Savitzky-Golay Filter? [Lecture Notes]. IEEE Signal Process Mag 2011;28(4):111–7. https://doi.org/10.1109/msp.2011.941097.
[49] Jonkman J, Butterfield S, Musial W, Scott G. Definition of a 5-MW reference wind turbine for offshore system development. National Renewable Energy Laboratory, 2009.
[50] Abbas NJ, Jasa J, Zalkind DS, Wright A, Pao L. Control co-design of a floating offshore wind turbine. Appl Energy 2024;353. https://doi.org/10.1016/j.apenergy.2023.122036.
[51] Poureh A, Chamani M, Bahri A. Nonlinear analysis of gain scheduled controllers for the NREL 5-MW turbine blade pitch control system. Int J Electr Power Energy Syst 2023;145. https://doi.org/10.1016/j.ijepes.2022.108578.
[52] Wang X, Zhou J, Qin B, Guo L. Coordinated control of wind turbine and hybrid energy storage system based on multi-agent deep reinforcement learning for wind power smoothing. J Storage Mater 2023;57. https://doi.org/10.1016/j.est.2022.106297.